ACS APPLIED MATERIALS & INTERFACES

Research Article

Cite This: ACS Appl. Mater. Interfaces 2018, 10, 39363−39379

www.acsami.org

Alkali Metal Cation Effects in Structuring Pt, Rh, and Au Surfaces through Cathodic Corrosion

Thomas J. P. Hersbach,[†] Ian T. McCrum,[†] Dimitra Anastasiadou,[†] Rianne Wever,[†] Federico Calle-Vallejo,[‡] and Marc T. M. Koper*,[†]

[†]Leiden Institute of Chemistry, Leiden University, P.O. Box 9502, 2300 RA Leiden, The Netherlands

[‡]Departament de Ciència de Materials i Química Fisica & Institut de Química Teòrica i Computacional (IQTCUB), Universitat de Barcelona, Martí i Franquès 1, 08028 Barcelona, Spain

Supporting Information

ABSTRACT: Cathodic corrosion is an electrochemical etching process that alters metallic surfaces by creating nanoparticles and a variety of etching features. Because these features typically have a preferential orientation, cathodic corrosion can be applied to modify and nanostructure electrode surfaces. However, this application of cathodic corrosion is currently limited by an insufficient chemical understanding of its underlying mechanism. This includes the role of alkali metal cations, which are thought to be crucial in both enabling cathodic corrosion and controlling its final facet preference. This work addresses this knowledge gap by exploring the cathodic corrosion of Pt, Rh, and Au in LiOH, NaOH, and KOH through both experimental and theoretical methods. These methods demonstrate that cations are adsorbed during cathodic corrosion and play a major role in controlling the onset potential and final surface morphology in cathodic corrosion. Interestingly, an equally significant role appears to be played by adsorbed hydrogen, based on calculations using literature density functional theory data. Considering the significance of both hydrogen and electrolyte cations, it is hypothesized that cathodic corrosion might proceed via an intermediate ternary metal hydride. This fundamental insight leads to both metal-specific recommendations and more general guidelines for applying cathodic corrosion to structure metallic surfaces.

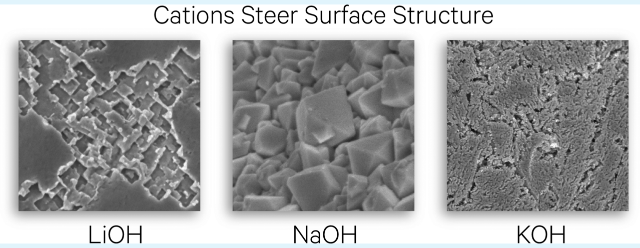

KEYWORDS: *cathodic corrosion, cation effects, electrolyte effects, electrode structuring, surface morphology, cation adsorption, hydrogen adsorption, ternary metal hydrides*

INTRODUCTION

Cathodic corrosion is an enigmatic etching process that decomposes metallic cathodes at potentials where they are typically assumed to be cathodically protected. This decomposition leads to striking changes in the electrode surface, including the formation of nanoparticles and geometric etch pits. Although these remarkable changes were already observed in the early 20th century[1] and briefly studied in the 1970s,[2] most fundamental studies of cathodic corrosion have been conducted relatively recently.[3−5] From these studies, it has been hypothesized that cathodic corrosion proceeds by forming an unknown metastable metal-containing anion,[6] instead of being caused by physical processes like contact glow discharge.[7] However, the exact nature of this (anionic) cathodic corrosion intermediate remains unclear. This limits fundamentally guided approaches toward applying cathodic corrosion to alter metallic surfaces and produce shape-controlled nanoparticles that exhibit favorable catalytic properties.[8] Such approaches would require more knowledge on the underlying mechanism and the different species involved in cathodic corrosion.

Perhaps the most crucial species in enabling cathodic corrosion is the electrolyte cation: without the presence of cations like Na^+, cathodic corrosion does not take place.[6] This key role of cations was underscored by several follow-up studies on nanoparticle production through cathodic corrosion, which reported effects of both the concentration and identity of the electrolyte cation on the corrosion rate,[9] particle size,[9−11] and particle shape.[9,12,13] In terms of particle shape, these experiments found the (100)-to-(110) facet ratio to increase with increasing cation concentration,[9,12,13] and being higher for particles produced in 10 M NaOH compared to 10 M KOH.[12] These observations were tentatively ascribed to selective stabilization of (100) surface facets by Na^+ adsorption;[13] Na^+ would mimic the structure-influencing effect that other adsorbates exhibit in traditional nanoparticle synthesis methods.[14] In spite of the pronounced effect of Na^+, these observations were made for alternating current (AC) corrosion experiments, which accelerate the effects of

Received: August 15, 2018
Accepted: October 23, 2018
Published: October 23, 2018

DOI: 10.1021/acsami.8b13883
ACS Appl. Mater. Interfaces 2018, 10, 39363−39379

cathodic corrosion by introducing periodic anodic corrosion steps. Although this approach is ideal for nanoparticle production, the convoluted presence of anodic and cathodic corrosion processes hinders explicit conclusions on the role of Na^+.

This ambiguity was alleviated by two subsequent studies on electrodes that were corroded under constant polarization.[15,16] These studies found that cathodic corrosion in 10 M NaOH preferentially forms (100) sites on Pt and Rh and (111) sites on Au. By exploring this difference between Au on the one hand and Pt and Rh on the other hand with density functional theory (DFT) calculations, sodium was shown to adsorb most favorably on the type of step that matches the type of site formed: (100) for Pt and Rh, and (111) for Au.[16] These results therefore align with the results on AC corrosion by suggesting a crucial role of the electrolyte cation in determining the facet preference for cathodic corrosion. However, a systematic study of the extent of this cation effect on various metals has previously not been conducted. Such a study would provide not only fundamental insights into cathodic corrosion but also concrete guidelines for using cathodic corrosion as a tool to structurally alter metallic electrodes.

Therefore, the work presented here provides such a study by mapping the corrosion behavior of Pt, Rh, and Au in various concentrations of LiOH, NaOH, and KOH. The experiments indicate a key role of the electrolyte cations in controlling the corrosion onset potential, as well as the final surface area and facet distribution of the corroded electrodes. Although these results do not allow us to determine a single reaction mechanism with certainty, the calculations do provide strong indications for the presence of adsorbed cations during cathodic corrosion. Additional calculations based on literature DFT data indicate an additional role of adsorbed hydrogen in determining the onset potential of cathodic corrosion. Given the suggested role of both adsorbed hydrogen and adsorbed cations, we will argue that the elusive cathodic corrosion reaction intermediate might be a ternary metal hydride.

These results are relevant from both fundamental and applied perspectives. On the one hand, the suggested existence of ternary metal hydrides provides a concrete starting point for future fundamental studies and is therefore an important clue toward understanding the chemical nature of cathodic corrosion. On the other hand, the exploration of cathodic corrosion as a function of the corroded metal and the identity and concentration of electrolyte cations provides valuable guidelines for applying cathodic corrosion to systematically modify electrode surfaces and create shape-controlled nanoparticles.

■ MATERIALS AND METHODS

Experimental Methods. Water used in this study was demineralized and filtered by a Milli-Q water system to reach a final total organic carbon content below 5 ppb and a resistivity above 18.2 MΩ cm. To further ensure cleanness, both organic and inorganic contaminations were removed from the glassware before each experiment. Organic contaminations were decomposed by storing the glassware overnight in an aqueous solution of 1 g L^{-1} $KMnO_4$ (Fluka, ACS reagent) and 0.5 M H_2SO_4 (Fluka, ACS reagent). After storage, the solution was drained from the glassware and any remaining $KMnO_4$ was removed with dilute H_2O_2 (Merck, Emprove exp). Finally, the glassware was boiled five times in water before being filled with electrolyte solution. All electrolytes were purged from oxygen before experiments by bubbling argon (Linde, 6.0 purity) through the solution for 30 min. Deoxygenation was maintained during experiments by flowing Ar over the solution. Electrochemical experiments were performed using a Bio-Logic SP-300 potentiostat.

In this study, two types of electrochemical cells were used: a glass cell for electrode characterization in acidic solution and a fluorinated ethylene propylene (FEP) cell for cathodic corrosion in alkaline solution. The glass cell contained an internal reversible hydrogen electrode (RHE) as reference electrode. The counter electrode was either a Pt spiral for Pt and Rh characterization or an Au spiral for Au characterization. In addition, a Pt or Au wire was connected to the reference electrode with a 4.7 μF capacitor to filter high-frequency noise during voltammetry.[17] Working electrolytes consisted of H_2SO_4 (Merck, Ultrapur) in concentrations of 0.5 mol L^{-1} for Pt or 0.1 mol L^{-1} for Rh and Au characterization. The FEP cell contained a commercial HydroFlex RHE electrode (Gaskatel), a Ti spiral counter electrode (MaTecK, 99.99%) and aqueous electrolytes of dissolved $LiOH{\cdot}H_2O$ (Alfa Aesar, 99.995%), NaOH (Merck, Suprapur), or $KOH{\cdot}H_2O$ (Fluka, TraceSelect).

The Ti counter electrode provides the important benefit of not being any of the studied working electrode materials. As such, the results presented in this work cannot be attributed to redeposition of dissolved Pt, Rh, or Au from the anodically polarized counter electrode. However, the use of a Ti counter electrode caused a noteworthy complication for cathodic corrosion, which we found to be very sensitive to the presence of unintended contaminations: for unknown reasons, the Ti counter electrode would occasionally shift the onset potential of cathodic corrosion of platinum to less negative potentials by as much as 0.3 V from the previously reported value.[15] This issue could generally be solved by performing 10 min of preelectrolysis at −1 V versus RHE with a Pt electrode (MaTecK, 99.99%; Ø = 0.1 mm), which was removed under potential control and discarded. Although this protocol adequately resolved the issue of early and significant cathodic corrosion, results of Pt corrosion were reproduced with a Pt counter electrode where necessary to confirm the validity of the presented onset potentials and the proper functioning of the working setup.

After preparing the working setup, Pt electrodes were prepared by cutting a short length of wire (MaTecK, 99.99%; Ø = 0.1 mm) from a spool with clean wire cutters and flame annealing the electrode. Rh (MaTecK, 99.9%; Ø = 0.125 mm) and Au (Materials Research Corporation, März Purity; Ø = 0.125 mm) wires could not be annealed before experiments and were cleaned chemically by immersion in a 1:3 volumetric mixture of 35% H_2O_2 (Merck, Emprove exp) and 95−97% H_2SO_4 (Fluka, ACS reagent) for 30 s instead.[16] Au wires were then also polished electrochemically by running 200 cyclic voltammograms (CVs) between 0 and 1.75 V versus RHE at a scan rate of 1 V s^{-1} in the characterization cell.[18]

After preparation, each electrode was immersed in the characterization cell at a depth that was carefully controlled by using a micrometer screw. In the characterization cell, the electrode surface was characterized by running four cyclic voltammograms. Following characterization, the electrode was rinsed and moved into the FEP cell. Here, an 85% ohmic drop-corrected constant cathodic voltage was applied for 60 s, after which the electrode was removed under potential control. After an additional rinse, the electrode was moved back into the characterization cell, immersed at the same depth as during the initial characterization, and recharacterized by running four CVs. Finally, the electrode was stored for later characterization using scanning electron microscopy (SEM).

Scanning electron microscopy was carried out on an FEI NOVA NanoSEM 200 microscope, using an acceleration voltage of 5 kV and an electron beam current of 0.9 nA. All samples were mounted to be aligned vertically in the presented micrographs, to within an error of several degrees.

Computational Methods. We used density functional theory to examine the specific adsorption of alkali metal cations (Li, Na, and K) onto the (111), (100), (211), and (553) surfaces of Rh, Pt, and Au in the presence of near-surface solvation. The Vienna Ab Initio Simulation Package was used to perform the electronic structure calculations,[19−21] with a plane-wave basis set and the Perdew−Burke−Ernzerhof (PBE) exchange-correlation functional.[22,23] Ioncore potentials were modeled using the projector augmented wave approach.[24,25] The basis set cutoff energy was 450 eV. Structural optimization was performed until the forces on the atoms were below 0.02 eV Å^{-1}. Adsorption was modeled at only one coverage. The (111) surface was modeled with a 3 × 3 unit cell (with three alkali metal cation adsorbates giving a 1/3 monolayer (ML) coverage), the (100) surface with a 2 × 2 unit cell (with one alkali metal cation adsorbate, 1/4 ML coverage), and the (211) and (553) surfaces in a 2 × 1 unit cell (containing a two-atom-wide step edge, with one alkali metal cation adsorbate). *k*-Space sampling was performed with a 5 × 5 × 1 Monkhorst−Pack mesh grid for the (111) surfaces of Rh and Pt and a 7 × 7 × 1 grid for all of the other surfaces of Rh and Pt.[26] The Au surfaces were sampled with a denser grid, 7 × 7 × 1 for Au(111), 11 × 11 × 1 for Au(100), 15 × 11 × 1 for Au(553), and 11 × 15 × 1 for Au(211). Adsorption energies on each surface were converged to within 0.03 eV with respect to the *k*-space sampling. Each of the surfaces was modeled with a four-layer slab, with the bottom two layers frozen at the DFT-calculated lattice constant. Dipole corrections were included in the surface normal direction.[27]

Cation adsorption potentials were calculated following methods described previously, including the effect of near-surface water solvation.[28,29] For the (111) surface, six explicit water molecules were included in a bilayer structure; for the (100), (211), and (553) surfaces, four explicit water molecules were added in a hydrogen-bonded monolayer adsorbed on the surface (or step edge, in the case of the stepped surfaces). Only one water structure was considered on each surface, which was relaxed in the absence and presence of the alkali metal cation. The initial water structures have been found previously (on Pt) to be low- or minimum-energy structures: on the (111) surfaces, a hexagonal bilayer water structure was used;[30,31] on the (100) surfaces, a squarelike arrangement of water molecules was used;[32] and on the stepped surfaces, a double-stranded structure was used.[33] Images of these structures, in the absence and presence of an alkali metal cation, are shown in Figures S1−S3. Images of the adsorbate structures were rendered using VESTA.[34]

This method approximates effects of solvation, since we can only identify water structures near the surface and the adsorbed cation that are at a local (but not necessarily global) minimum in energy, and we neglect translational and rotational entropy of the near-surface water (considering only vibrational energy and entropy). Our intent is therefore to only approximate the effects of near-surface solvation on the alkali metal cation adsorption energy. In our prior work, we found this energy to reach a plateau after solvating the adsorbed cation with four to six water molecules:[28] approximately the number of water molecules in the solvation shell of bulk, solution-phase alkali atoms, as found previously using ab initio molecular dynamics.[35] We found previously that the addition of more water molecules causes the absolute alkali metal adsorption energy to fluctuate by ±0.5 eV per water molecule. We therefore expect our absolute adsorption energy accuracy to not be better than ±0.5 eV. The error in the relative adsorption energy trend between cations is smaller.

Adsorption energies were also calculated in the absence of near-surface solvation and relative to gas phase, neutral alkali metal atoms, following a method described previously.[16] These calculations neglect the stabilizing effect of solvent on both the reactant and adsorbed product states. This alters both the absolute adsorption energetics and the trend between the cations because the degree of lost solvation upon adsorption is cation-dependent. These adsorption energies are given in the Supporting Information (SI) (Figures S30 and S31) and allow for separate examination of the contribution of the solvation effects on adsorption. Figures S30 and S31 can be compared to the adsorption energetics in the main text, which are all calculated using an aqueous solution-phase ion as the initial state.

Cation effects have been explained as being caused by the behavior of cations in the double-layer or outer Helmholtz plane, near the electrode surface.[36] However, we here examine the conditions under which some of these cations approach the electrode surface more closely and lose part of their solvation shell. This allows them to be considered "specifically adsorbed". Our current and previous calculations therefore support that such adsorption is favorable at low potentials and high pH,[28,37] where alkali cation adsorption becomes increasingly favorable compared to hydrogen adsorption.

We have also examined the stability of the (111) and (100) surfaces of Rh, Pt, and Au in the presence of high coverages of adsorbed hydrogen, using bare surface energies calculated using DFT by Tran et al.,[38] as well as hydrogen adsorption energies calculated using DFT at low coverage (0.25 ML) by Ferrin et al.[39] To estimate the adsorption energy of hydrogen at high coverages, we assumed a simple mean-field model using a constant, repulsive, coverage dependence of the hydrogen adsorption energy of 0.12 eV ML^{-1} on the (111) surfaces of Rh, Pt, and Au. This repulsive interaction has been explicitly calculated on Pt(111);[29,40] the same coverage dependence was assumed on Rh(111) and Au(111). It should be noted that Skúlason et al. show a slightly greater repulsion on Au(111) and weaker repulsion on Rh(111) than on Pt(111).[41] Consideration of these differences would yield a small change in the calculated surface energetics at low potentials (high hydrogen coverages). However, this change would only emphasize the trend in which (111) surface is the most stable (Rh > Pt > Au). As such, including these small differences in binding energy (BE) will not affect our conclusions. We also assume that adsorption between low and high coverage (1 ML) on the (100) surfaces is independent of coverage on Rh(100), Pt(100), and Au(100), as has been found for Pt(100).[29,40] Potential-dependent surface energies (with 1 ML hydrogen adsorbed on the surface) were calculated as described previously, by adding the potential-dependent adsorption energy of hydrogen (normalized by surface area) to the surface energy of the bare surface.[42] This procedure is outlined in eqs 1 and 2

$$\gamma(U_{\mathrm{RHE}}, \theta_{\mathrm{H}*}) = \gamma_{\mathrm{bare}} + \frac{\Delta G_{\mathrm{H_{ads}}}(U_{\mathrm{RHE}}, \theta_{\mathrm{H}*})}{A} \tag{1}$$

$$\begin{aligned} \Delta G_{\mathrm{H_{ads}}}(U_{\mathrm{RHE}}, \theta_{\mathrm{H}*}) &= \mathrm{BE}(\theta_{\mathrm{H}*} = 0.25\ \mathrm{ML}) + 0.5\Delta H_{\mathrm{H_2}}^{\mathrm{form}} \\ &\quad + \Delta \mathrm{ZPVE}_{\mathrm{H_{ads}}} - T\Delta S_{\mathrm{H_{ads}}} + n|e|U_{\mathrm{RHE}} + \omega\theta_{\mathrm{H}*} \end{aligned} \tag{2}$$

where $\gamma(U_{\mathrm{RHE}},\theta_{\mathrm{H}*})$ is the surface energy of the hydrogen-covered surface as a function of potential (on a reversible hydrogen electrode (RHE)) scale and hydrogen coverage ($\theta_{\mathrm{H}*}$), γ_{bare} is the surface energy of the bare surface,[38] A is the area of the surface, $\Delta G_{\mathrm{H_{ads}}}(U_{\mathrm{RHE}},\theta_{\mathrm{H}*})$ is the free energy of hydrogen adsorption, BE is the binding energy of hydrogen on the surface at low coverage (0.25 ML),[39] $\Delta H_{\mathrm{H_2}}^{\mathrm{form}}$ is the formation enthalpy of hydrogen gas at standard state (−4.57 eV),[39] $\Delta\mathrm{ZPVE}_{\mathrm{H_{ads}}}$ is the change in zero point vibrational energy of the hydrogen upon adsorption (−0.008 eV),[40] $T\Delta S_{\mathrm{H_{ads}}}$ is the change in entropy of the hydrogen upon adsorption (−0.00067 eV K^{-1}),[40] n is the number of hydrogen atoms adsorbed in the unit cell at the coverage of interest, $|e|U_{\mathrm{RHE}}$ is the energy of an electron on the reversible hydrogen electrode scale, and ω is the H*−H* interaction term describing the interaction between adsorbed hydrogen on the surface (0.12 eV ML^{-1} for H* on Pt(111), ∼0 eV ML^{-1} for H* on Pt(100)).[29,40] This difference in interaction energy is consistent with experimental estimates that indicate weaker (but nonzero) H−H interactions for Pt(100) than for Pt(111).[43,44] We assumed complete electron transfer between the adsorbing proton and the surface, so that all of the potential dependence arises from the electron being transferred as a reactant on proton adsorption. Additionally, we neglected the effects of near-surface solvation and electric field on hydrogen adsorption, since these effects have been shown previously to be small.[40]

As we have found hydrogen adsorption above 1 ML (up to 1.25 ML) on Pt(100) to be favorable at low but positive potentials (near 0.1 V vs RHE),[42] we have extrapolated and included these data as well. Besides, we calculated the adsorption energy of hydrogen at 1.25 ML on Rh(100) using the same methods defined previously for H* adsorption on Pt(100).[42] For this calculation, we used the PBE exchange-correlation functional, as was used to examine alkali metal cation adsorption. We find that the additional 0.25 ML hydrogen prefers to adsorb in a bridge site (as do the hydrogen atoms between

0 and 1 ML) on Rh(100). As hydrogen adsorption is significantly weaker on Au(100) than on Pt(100) and Rh(100), a higher coverage (1.25 ML) was not considered on this surface.

While the bare surface energies are particularly sensitive to the functional used and the level of convergence defined, the relative stability of the (111) and (100) facets of each metal should be less sensitive. We therefore expect the trend in surface energies between (111) and (100) to be robust.

■ RESULTS

In the following section, we will first describe the experimentally studied corrosion behaviors of Pt, Rh, and Au in LiOH, NaOH, and KOH electrolytes. This description will be separate for each metal and will focus on the difference in corrosion behavior as a function of the electrolyte composition. This approach differs slightly from our previous work, which mainly described the corrosion behavior as a function of the corrosion potential.[15,16] However, an electrochemical impression of the corrosion behavior as a function of the applied potential can be gained from Figures S4−S15 in the Supporting Information (SI), which correspond to the figure format used in our earlier work. Similarly, Figures S16−S27 display scanning electron micrographs of the electrodes as a function of the applied potential. Since Figures S4−S27 are designed to complement the figures in the main article, the interested reader is referred to the supporting figures for a more complete impression of the experimental results on the corrosion behavior of the studied systems. These figures in the SI are also accompanied by additional discussion of the presented results and conclusions.

After describing the experimental results, we will proceed by presenting our complementary theoretical results on the adsorption of Li, Na, K, and H on Pt, Rh, and Au. The experimental and theoretical results will be further interpreted and connected in the Discussion section.

Experimentally Determined Corrosion Behavior. The corrosion behaviors of Pt, Rh, and Au were studied through both cyclic voltammetry (CV) and scanning electron microscopy (SEM). As in our previous work, the metallic electrodes were treated by applying a constant cathodic voltage versus an internal reversible hydrogen electrode (RHE) for 60 s in a concentrated alkali metal hydroxide solution.[15,16] Before and after this cathodic polarization, the electrodes were characterized by cyclic voltammetry in a sulfuric acid solution to monitor changes in the structure of the electrode surface. Additionally, the electrodes were imaged by SEM after corrosion to identify etching features in the surface.

In these experiments, the applied corrosion potentials are purposefully spaced by 0.1 V steps: the smallest interval at which we believe that differences in corrosion behavior can reliably be assessed with the current methodology. Given this potential spacing, our resolution in determining corrosion onset potentials is 0.1 V. Strictly speaking, this means that the "true" corrosion onset potential will lie between the most negative potential where no corrosion can be detected and the least negative potential where corrosion can be detected. For consistency, however, we will follow our previous work in defining the corrosion onset potential as the least negative potential where corrosion can be detected.[15] This detection will rely predominantly on cyclic voltammetry.

Platinum. For platinum, the use of cyclic voltammetry is well established as a quick and reliable method for characterizing electrode surfaces. This characterization relies on the so-called "hydrogen region", which in 0.5 M H_2SO_4 contains the following anodic features that are important for this work:[45]

1. A peak at 0.13 V vs RHE, corresponding to the substitution of H* by OH* on (110)-type sites.[46,47]
2. A peak at 0.27 V vs RHE, corresponding to (100)-type step sites near terrace borders.[46,47]
3. A broader feature between 0.3 and 0.4 V vs RHE, corresponding to (100) terrace sites.
4. A broad feature between 0.06 and 0.3 V vs RHE, corresponding to hydrogen desorption on (111) terraces. This feature is accompanied by a broad feature between 0.4 and 0.55 V vs RHE, for (bi)sulfate adsorption on (111) terraces.

Since these features depend strongly on the presence and extent of their corresponding surface sites, the use of cyclic voltammetry is extremely sensitive to small changes in the electrode structure. As such, CV measurements, complemented by SEM images, will be the primary method for quantifying the differences between corrosion in different electrolytes.

Electrolyte Concentration. The differences are first explored as a function of cation concentration for NaOH electrolytes: in Figure 1, voltammograms of electrodes corroded at −1 V versus RHE in 1, 5, and 10 M NaOH are displayed in increasingly darker colors, with the uncorroded electrode displayed in dark blue. The comparison of these voltammograms reveals higher measured currents in the voltammograms of electrodes corroded in higher NaOH concentrations. This higher current corresponds to a larger hydrogen desorption charge, which in turn corresponds to more exposed surface area.[48] For the presented samples, this represents surface area increases of 28, 32, and 74% after corrosion in 1, 5, and 10 M NaOH, respectively. Higher electrolyte concentrations therefore induce more electrode roughening.

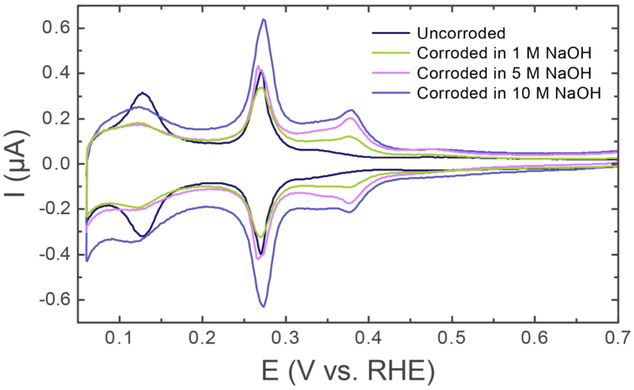

Figure 1. Cyclic voltammograms of Pt corroded in NaOH of various concentrations, at −1.0 V vs RHE. Voltammograms were recorded in 0.5 M H_2SO_4 at a scan rate of 50 mV s^{-1}.

This increased roughness with increasing concentration correlates well with the corrosion onset potential. For Pt corrosion, this onset is signified by a decrease in (110) features at 0.13 V versus RHE, which is accompanied by a minor increase in (100) features at 0.27 V versus RHE.[15] As can be seen in Figures S5 and S8, these changes occur, respectively, after polarization at −0.6 V versus RHE (−1.4 V vs NHE) and −0.5 V versus RHE (−1.4 V vs NHE) in 1 and 5 M NaOH. These onset potentials are more negative than the −0.4 V

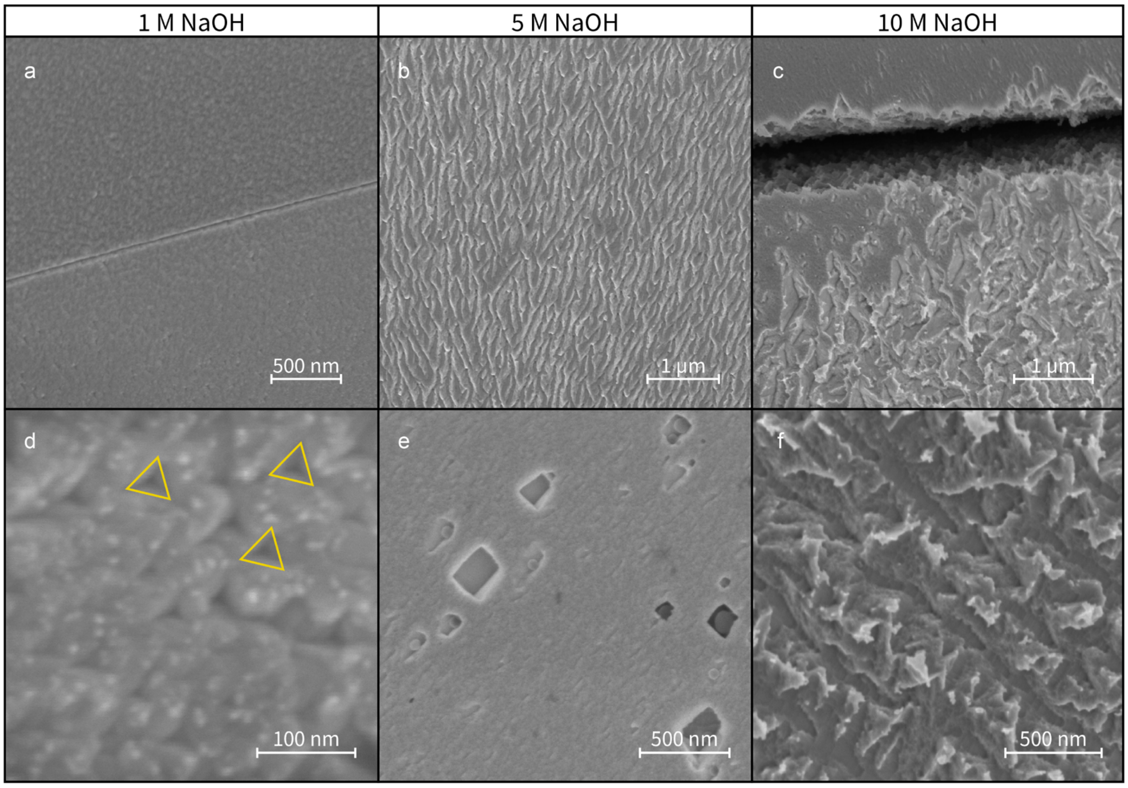

Figure 2. Scanning electron micrographs of Pt electrodes corroded at −1 V vs RHE in 1 M NaOH (a, d), 5 M NaOH (b, e), and 10 M NaOH (c, f). Triangular features are highlighted in yellow.

versus RHE (−1.3 V vs NHE) observed in 10 M NaOH.[15] This onset trend and the less substantial roughening in more dilute solutions indicate that the extent of corrosion correlates strongly with NaOH concentration.

Based on this trend as a function of concentration, one might expect the facet distribution to also change monotonically with regard to concentration. This is indeed the case for (100) features: both (100) step sites (0.27 V vs RHE) and terrace sites (0.3−0.4 V vs RHE) increase with electrolyte concentration. However, the amount of (110) sites first decreases between 1 and 5 M NaOH and then increases when corroding in 10 M NaOH. This indicates an interesting feature of cathodic corrosion in 10 M NaOH: the newly created surface area appears more disordered than that created at lower electrolyte concentrations, as is motivated in the SI.

Further indications of a rougher and more disordered surface follow from microscopy-based examination of the corroded electrodes, presented in Figure 2. In this figure, panels (a) and (d) display an electrode corroded in 1 M NaOH at −1.0 V versus RHE. As can be seen in panel (a), which features the boundary between two crystal grains, the electrode appears predominantly roughened on the nanoscale, without the presence of well-defined etching features. However, small sections of the electrode feature triangular etch pits, which are (100)-oriented pits in (111)-like facets (model etch pit: Figure S28).[15]

More severe corrosion features are present after cathodic treatment at −1 V vs RHE in 5 M NaOH (Figure 2b,e). This treatment causes the appearance of etch lines (Figure 2b) on large sections of the electrode and areas containing etch pits with more subtle roughening between them (Figure 2e). Many of these pits contain ~90° angles and are assigned to (100)-type sites. This assignment is based on previous work, but is also illustrated here by a model etch pit (Figure S28).[15]

Finally, when increasing the NaOH concentration to 10 M (Figure 2c,f), the etch features increase further in size, thus indicating higher roughness. These features (Figure 2f) contain edges that are less straight than those after corrosion in less concentrated solutions. As such, the SEM images support the electrochemical observation that the increase from 5 to 10 M NaOH induces the formation of more disordered sites on the nanolevel. Similarly, the SEM results corroborate the electrochemically observed roughness increase with cation concentration.

Cation Identity. Besides being sensitive to the cation concentration, cathodic corrosion also responds strongly to the cation identity. This is illustrated in Figure 3, which explores Pt corrosion as a function of cation type for electrolyte concentrations of 1 M (panels (a) and (b)) and 5 M (panels (c) and (d)). This exploration is further subdivided in mildly negative potentials (panels (a) and (c)) and more negative corrosion potentials (panels (b) and (d)).

At mildly negative potentials, the electrolyte cation appears to barely affect the facet preference after corrosion. At these potentials, the cyclic voltammograms for corroded Pt overlap quite well: the amount of created (100) terraces is similar for all electrolytes of similar concentrations. This overlap is particularly noteworthy because the corrosion onset potentials, derived from Figures S4−S9, are not the same for all types of cations. For 1 M KOH, the onset potential is −0.5 V versus RHE (−1.3 V vs NHE), while it is −0.6 V versus RHE (−1.4 V vs NHE) for 1 M NaOH and LiOH. Similarly, for 5 M electrolytes, the onset potential is −0.4 V versus RHE (−1.3 V vs NHE) for KOH and at −0.5 V versus RHE (−1.4 V vs NHE) for NaOH and LiOH. This indicates that, at mildly

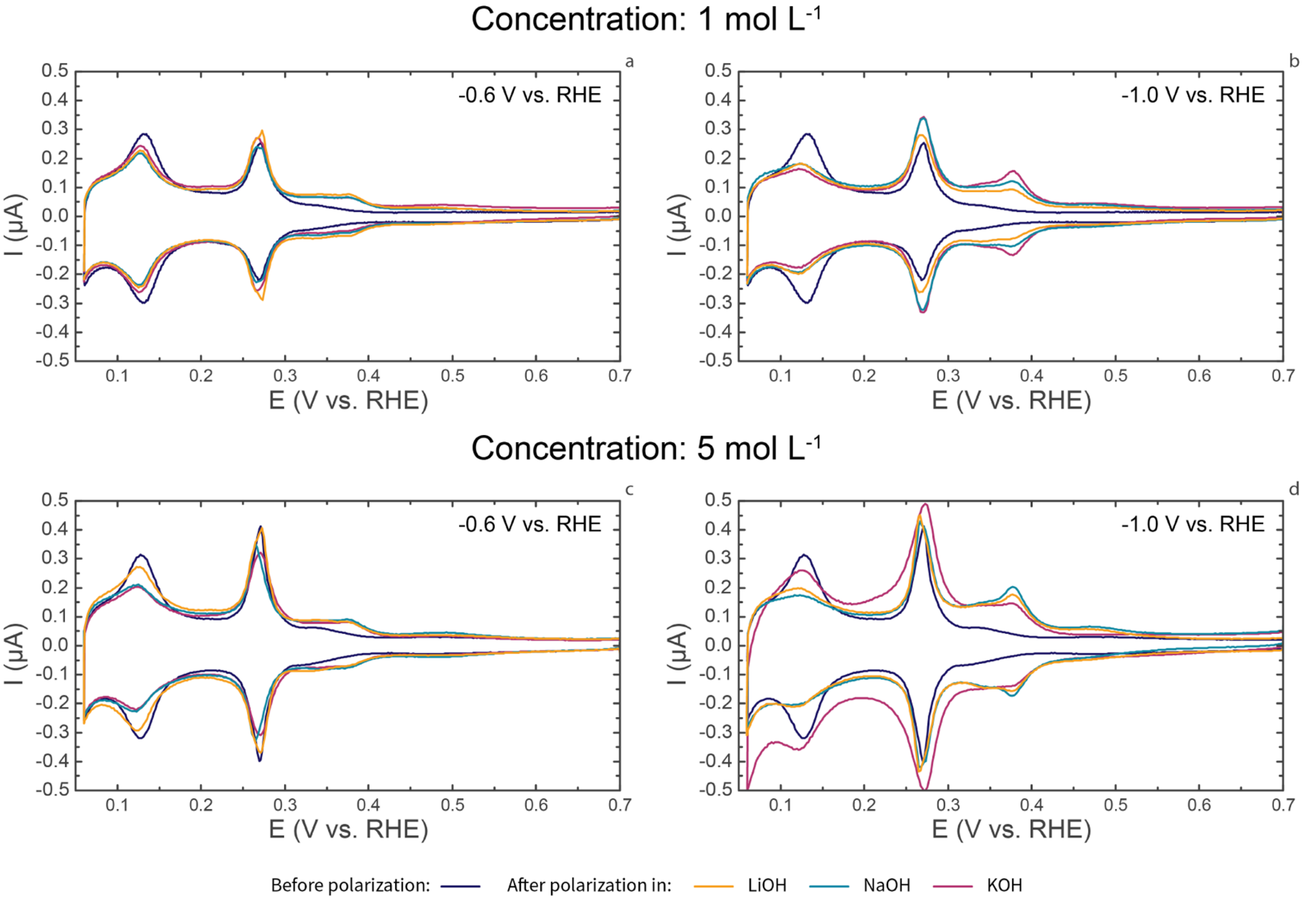

Figure 3. Cyclic voltammograms of Pt corroded in LiOH, NaOH, and KOH at concentrations of 1 M (a, b) and 5 M (c, d), at −0.6 V vs RHE (a, c) and −1.0 V vs RHE (b, d). Voltammograms were recorded in 0.5 M H_2SO_4 at a scan rate of 50 mV s^{-1}.

negative potentials, the final facet distribution does not necessarily correlate with the cation-influenced onset potential, but rather with the applied electrode potential.

This observation contrasts with the behavior at more negative potentials, which depends strongly on the nature of the electrolyte cation. For 1 M corrosion electrolytes (Figure 3c), this dependence shows a clear trend between cations: larger cations remove more (110) sites and create more (100) step and terrace sites. This facet preference trend is accompanied by a modest tendency for more surface area creation as the cation size increases.

The trend in surface area formation is sustained in more concentrated solutions, as can be seen in Figure 3d: at −1 V versus RHE, most surface area is created in KOH solutions, followed by NaOH and LiOH. Similarly, the facet preference trend is almost sustained in 5 M solutions. As in more dilute solutions, slightly more (100) terraces are created in NaOH electrolytes than in LiOH electrolytes. However, compared to these electrolytes, KOH causes an increase in (110) and (100) step sites and a small decrease in (100) terraces. This increased step site formation is similar to that observed between 5 and 10 M NaOH. One can therefore also argue that moving from 5 M NaOH to 5 M KOH produces a more disordered surface after corrosion.

These electrochemical results can be analyzed in the light of scanning electron microscopy characterization. For 1 M electrolytes, SEM detects differences between cations, with larger cations inducing more corrosion (Figures S16−S18). This qualitatively matches the results in more concentrated electrolytes. As can be seen in Figure 4a and d, corrosion in 5 M LiOH causes the formation of (100)-type triangular etch pits. These pits are present on small areas of the electrode; in other areas, any corrosion feature is beyond the resolution of the SEM (Figure S19).

This differs significantly from corrosion in 5 M NaOH (Figures 2b,e and 4b,e): etch lines are widespread and rectangular etch features can be seen in Figure 2e, underneath the grain boundary in Figures 4b and S20e. In addition, the electrodes show significant corrugation that contains triangular features (Figure 4e), which resemble the triangular pits observed for less severe corrosion. These pits could therefore serve as initiation sites for more severe etching features, as is illustrated in the SI.

Finally, corroding in 5 M KOH creates rougher and less well-ordered features than those observed for LiOH and NaOH: large troughs are found along grain boundaries (Figure 4c) and significant roughness without straight features is found on crystal grains (Figure 4f).

These SEM and voltammetry results create a coherent impression of cathodic corrosion. Corrosion in LiOH creates the least amount of surface area. This area is only slightly smaller than that created in NaOH electrolytes, while the electrodes appear markedly different in SEM. This indicates that corrosion in LiOH electrolytes creates roughness on scales below the SEM resolution. Corrosion in NaOH electrolytes then causes more macroscopic roughness. This roughness contains well-developed electrochemical (100) terrace features that correspond to the formation of straight, long-distance

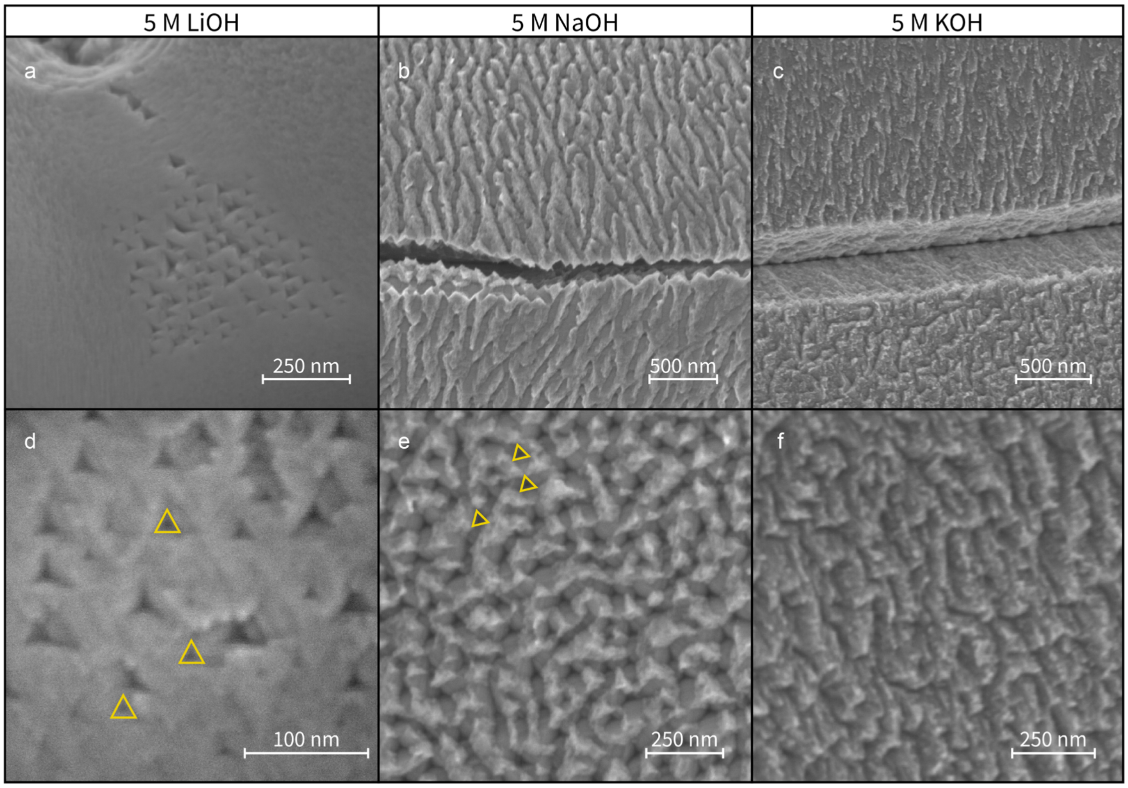

Figure 4. Scanning electron micrographs of Pt electrodes corroded at −1 V vs RHE in 5 M LiOH (a, d), 5 M NaOH (b, e), and 5 M KOH (c, f). Triangular features are highlighted in yellow.

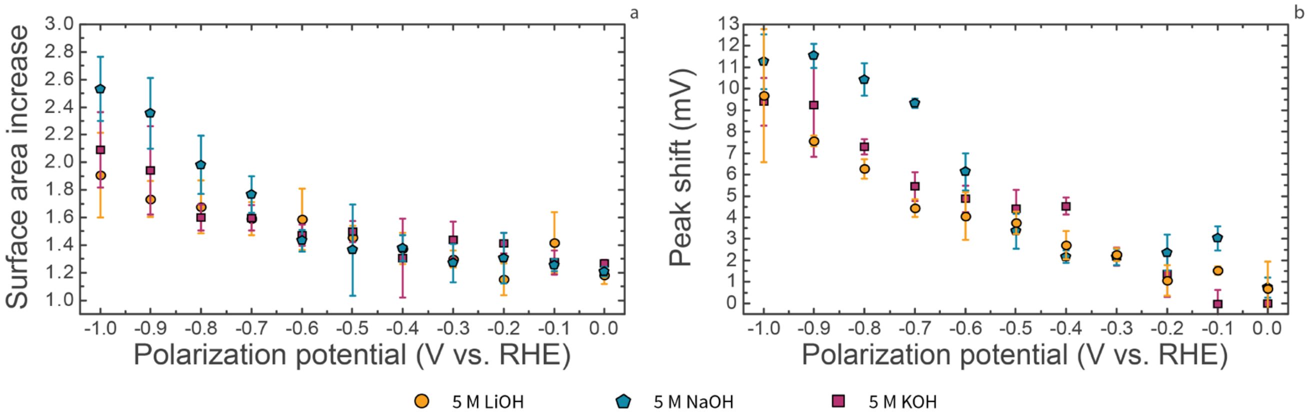

Figure 5. Relative rhodium surface area increase after cathodic polarization (a) and shift of the anodic hydrogen peak (b), as a function of the applied polarization potential in 5 M LiOH, 5 M NaOH, and 5 M KOH. Each data point is the average of at least three independent experiments. Error bars represent 1 standard deviation; if an error bar is not visible, it falls within its corresponding data point.

features in SEM. Such well-ordered sites are mostly absent from electrodes corroded in 5 M KOH, which appear the roughest and most disordered in both voltammetry and electron microscopy.

As such, a clear effect of the cation is present for both studied electrolyte concentrations. At low concentrations, the cation predominantly affects the surface facet distribution, causing most (100) sites to be formed in KOH, followed by NaOH and LiOH. At higher concentrations, corrosion in NaOH and LiOH induces well-developed (100) features, with KOH leading to an increased amount of step sites. Corrosion furthermore produces more surface area with increasing cation size.

Rhodium. In contrast to platinum voltammograms, rhodium voltammograms only feature one set of "hydrogen" peaks.[49] Of this set, the cathodic peak corresponds to (bi)sulfate desorption, accompanied by hydrogen adsorption. Accordingly, the anodic peak corresponds to hydrogen desorption, accompanied by (bi)sulfate adsorption. The position of these peaks varies, depending on the exposed electrode facets. For the three basal planes, this yields the following peak positions in 0.1 M H_2SO_4:

1. Rh(111) contains a sharp cathodic peak at 0.105 V vs RHE and a sharp anodic peak at 0.122 V vs RHE.
2. Rh(100) contains a sharp cathodic peak at 0.149 V vs RHE and a sharp anodic peak at 0.157 V vs RHE.

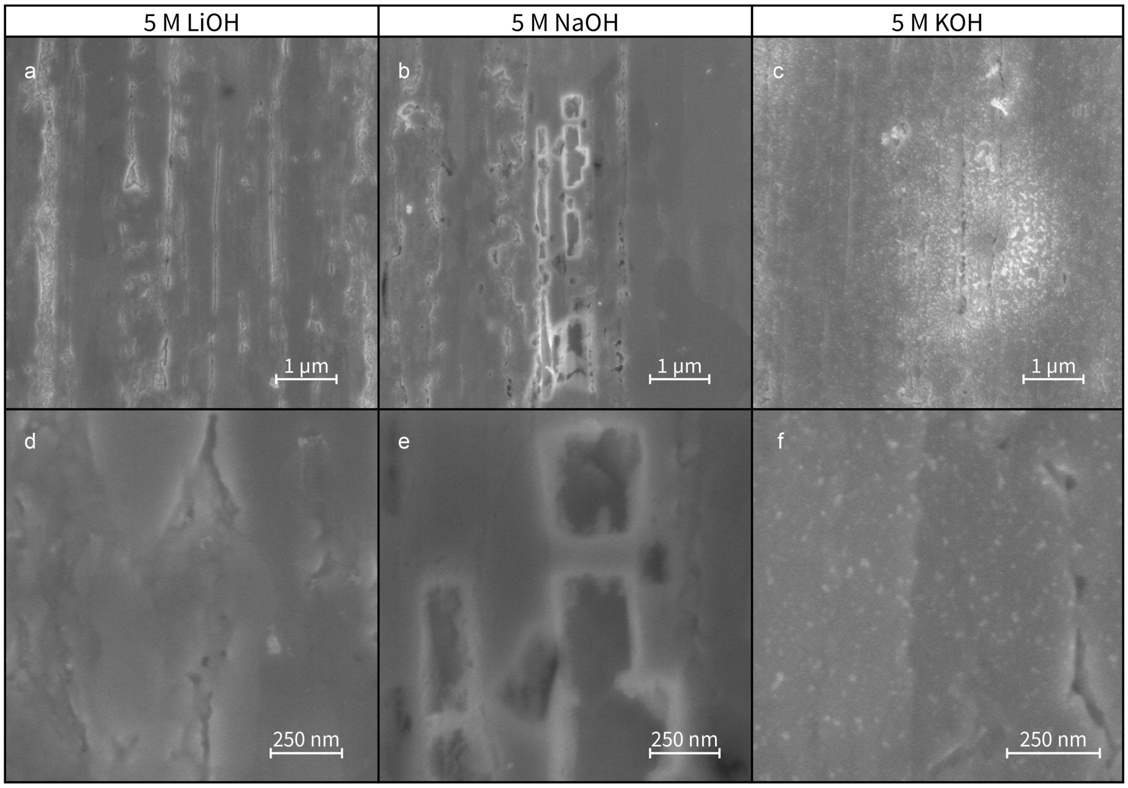

Figure 6. Scanning electron micrographs of Rh electrodes corroded at −1 V vs RHE in 5 M LiOH (a, d), 5 M NaOH (b, e), and 5 M KOH (c, f).

3. Rh(110) contains a broad cathodic peak at 0.107 V vs RHE and a broad anodic peak at 0.120 V vs RHE.

In line with our previous work,[16] we will primarily focus on the anodic peaks. The peaks are located around 0.121 V versus RHE for the (111) and (110) facets, but situated approximately 35 mV more positive for the (100) facet. We previously used this peak position difference to determine the onset potential of rhodium: at the corrosion onset of −0.4 V versus RHE (−1.3 V vs NHE), the anodic hydrogen peak shifts positively by 2 mV. This positive shift signifies the formation of (100) sites.[16] Because this peak shift is more abrupt than the gradual increase in electrode surface area, the same shift will be used here to determine the corrosion onset. We will focus exclusively on the effect of the cation identity in 5 M electrolytes because cathodic corrosion of Rh in 1 M electrolytes is subtle and the spread in the data is too large to reliably establish onset potentials and facet preferences.

Cation Identity. For 5 M electrolytes, the peak shift and surface area increase (as determined from the hydrogen desorption charge) after 60 s of cathodic polarization are presented in Figure 5. In this figure, the anodic peak shift (panel (b)) is approximately 2 mV in the absence of cathodic corrosion. Although this "baseline" shift is slightly higher than the <1 mV shift in our previous work,[16] it is reproducible for the presently studied electrolytes. The first electrolyte to exhibit a shift larger than 2 mV is 5 M KOH, for which a 4 mV peak shift marks the onset of cathodic corrosion at −0.4 V versus RHE (−1.3 V vs NHE). In agreement with previous work, this 4 mV change represents an approximate 2 mV shift from the baseline change in peak position. Similar 3−4 mV total shifts occur at −0.5 V versus RHE (−1.4 V vs NHE) for LiOH and NaOH. These onset potentials match those for Pt corrosion, with corrosion in 5 M KOH starting at less negative potentials than corrosion in 5 M NaOH and LiOH.

Another similarity with Pt is that the initial surface area increase (Figure 5a) is similar at mildly negative potentials and starts diverging at approximately −0.7 V versus RHE. However, the trend in surface area formation differs from platinum: most surface area is formed in NaOH, followed by KOH and LiOH. Although the cause of this differing trend is unclear, it does match the observed peak shifts for Rh corrosion: the shift is highest for NaOH, with LiOH and KOH producing shifts that are 2−4 mV smaller, depending on the exact corrosion potential.

Such differences between cations in both surface area and peak shift are consistent with SEM characterization results, which are shown for the three electrolytes in Figure 6. The electrolyte for which Figure 5a indicates the smallest surface area increase is 5 M LiOH. In electron microscopy (Figure 6a,d), Rh electrodes corroded in this electrolyte typically exhibit no signs of cathodic corrosion: with the exception of one electrode (Figure S22c), the electrodes only contain ridges and cracks that align with the electrode, which are not caused by cathodic corrosion.[16]

More signs of corrosion are visible for rhodium electrodes corroded in 5 M KOH (Figure 6c,f), which is the electrolyte that ranks second in surface area creation. Interestingly, this electrolyte does not cause the formation of large etch pits, but instead creates a high coverage of small particles that are attached to the surface.

Finally, small particles can be observed after corrosion in 5 M NaOH (Figure 6b,e) and large quasi-rectangular pits are found after corrosion at and below −0.9 V versus RHE. These pits match those created in 10 M NaOH and are assigned to (100) site formation.[16] They therefore match the CV peak

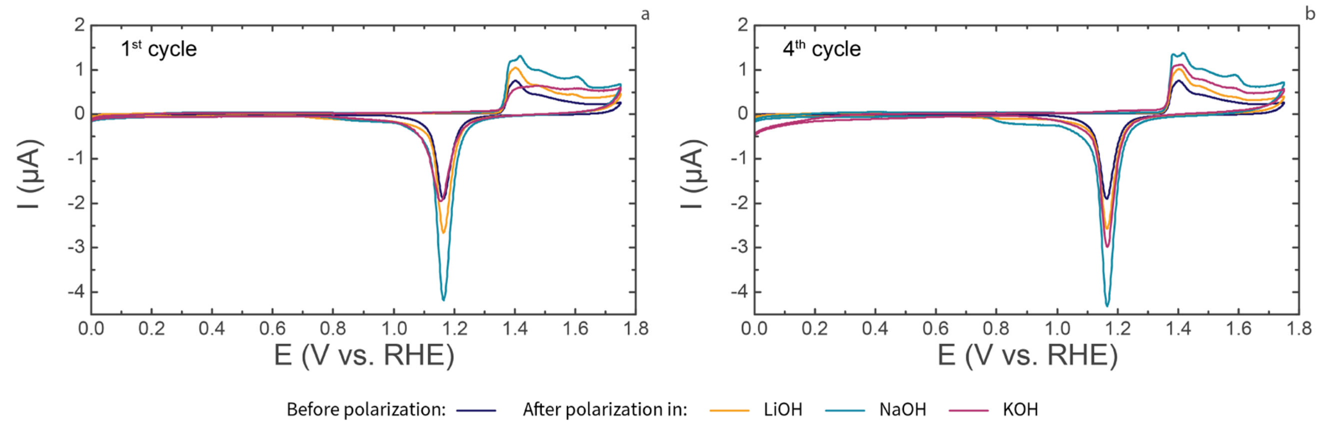

Figure 7. Cyclic voltammograms of Au, corroded in 5 M LiOH, 5 M NaOH, and 5 M KOH at −1.5 V vs RHE. Voltammograms shown are the first voltammogram (a) and the fourth voltammogram (b) after cathodic corrosion. Voltammograms were recorded in 0.1 M H_2SO_4 at a scan rate of 50 mV s^{-1}.

shift ((100) preference) in Figure 5 being highest for corrosion in NaOH. Additionally, the etch pits are the largest features observed for rhodium in this study, which correlates well with the electrochemical surface area increase being largest for 5 M NaOH.

Summarizing, both electrochemistry and electron microscopy indicate the surface area increase to be smallest for LiOH, followed by KOH and NaOH. Besides, electrochemistry indicates the largest amount of (100) sites to be formed in NaOH, which matches the occurrence of large, quasi-rectangular etch pits. Although these observations from CV and SEM lack the clear trends observed for platinum, both techniques produce mutually consistent results for the corrosion behavior of rhodium.

Gold. For gold, the change in surface orientation will be studied by using the oxide region in the cyclic voltammogram. This region is situated approximately between 1.35 and 1.75 V versus RHE and contains several overlapping peaks corresponding to the following three basal planes:[50,51]

1. Au(111) produces a peak at 1.58 V vs RHE.
2. Au(100) produces a peak at 1.42 V vs RHE.
3. Au(110) produces a peak at 1.46 V vs RHE.

Peaks corresponding to (100) and (111)/(110)-oriented steps are found at 1.39 and 1.43 V versus RHE.[50] Although some of the peaks are situated rather close to each other, they are reliable indicators of the amount of exposed basal planes.[18] The peaks will therefore be used to assess changes in the electrode surface after cathodic corrosion. As with rhodium, these changes are not reported for concentrations of 1 M; corrosion in these concentrations did not produce changes that were significant enough to reliably identify onset potentials and etching preferences.

Cation Identity. Larger changes are observed for experiments in 5 M alkali metal hydroxides. For corrosion in these electrolytes, voltammograms before and after corrosion at −1.5 V versus RHE for 60 s are shown in Figure 7. The figure shows both the first (panel (a)) and fourth (panel (b)) voltammetric cycles after cathodic corrosion because the electrode surface changes between cycles due to repetitive oxidation and reduction.[18] Such changes could obscure the difference between cations if only the fourth cycle were used for comparison. In addition, the displayed CVs are shown for a more negative corrosion potential (−1.5 V vs RHE) than those shown for rhodium and platinum. This is because corrosion is significantly milder for gold, which causes smaller differences between the cations at less negative potentials; voltammograms of electrodes polarized around the corrosion onsets and at −3.0 V versus RHE are available in Figures S13−S15.

At −1.5 V versus RHE, corrosion in all three electrolytes creates some extent of (111) features. These features, which are visible around 1.58 V versus RHE, can be used to identify the onset potential of gold corrosion.[16] This analysis is presented in Figure S29 and indicates the onset potentials to be −0.9 V versus RHE (−1.8 V vs NHE) for 5 M LiOH and −0.8 V versus RHE (−1.7 V vs NHE) for 5 M NaOH and KOH. As for platinum and rhodium, these potentials are 0.1−0.2 V more negative than the corrosion onset potential in 10 M NaOH: −0.7 V versus RHE (−1.6 V vs NHE).[16] This indicates a later onset of cathodic corrosion for all three cations in more dilute electrolytes.

When the facet preference of the cations is compared, several interesting features stand out. These features are most clearly visible in the first cycle after corrosion (Figure 7a). From this cycle, one can observe that LiOH induces the creation of only a small amount of (111) facets. Instead, the most-developed peak is the (100) peak at 1.41 V versus RHE. This also holds true after four cycles (Figure 7b), with only small changes occurring between cycles.

The corrosion behavior in 5 M LiOH is not matched by NaOH, which induces a strong development of (111) sites (1.58 V vs RHE) in both the first and fourth characterization cycles. An additional difference with respect to LiOH is the amount of created surface area, which can primarily be assessed by the size of the oxide reduction peak at 1.16 V versus RHE.[52] A larger peak after corrosion in 5 M NaOH indicates significantly more surface area formation than corrosion in 5 M LiOH.

Finally, the created surface area in 5 M KOH displays an interesting behavior with respect to the other two electrolytes. During the first cycle after corrosion, it appears that virtually no surface area has been created: the oxide reduction peak is similar in height to the peak of a pristine electrode. Interestingly, this peak grows in size during characterization after cathodic corrosion, leading to a CV similar to that after corrosion in 5 M LiOH, but with slightly more surface area, step sites, (110) terrace sites, and (111) sites. Although these changes are discussed in more detail in the SI, the current

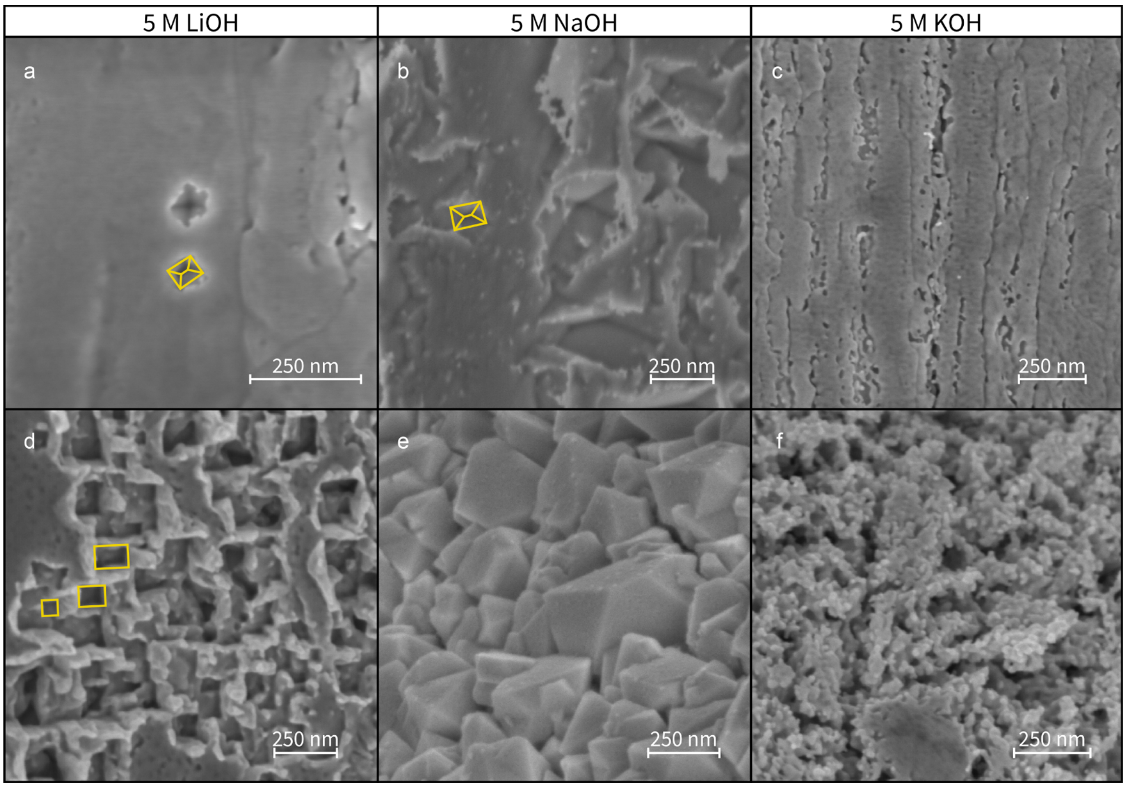

Figure 8. Scanning electron micrographs of Au electrodes corroded at −3 V vs RHE in 5 M LiOH (a, d), 5 M NaOH (b, e), and 5 M KOH (c, f). Images in (d)−(f) were taken at the tip of the electrode, whereas images in (a)−(c) were taken further away from the tip. Representative etch pits have been highlighted in yellow.

analysis already indicates a strong difference in corrosion behavior for different cations.

As for Pt and Rh, these voltammetric changes correspond to changes observed with SEM. Scanning electron micrographs are shown for corrosion at −3.0 V versus RHE in Figure 8. This potential was chosen for SEM comparison because no corrosion could be detected by SEM for gold in 5 M LiOH at −1.5 V versus RHE (Figure S25). For this electrolyte, corrosion features were only visible near the tip of the electrode. These features consist predominantly of etch pits, of which a particularly interesting example is shown in panel (a). This type of etch pit is highlighted in yellow: it has outlines that appear to have roughly 90° angles and pit walls that slant inwards. This type of pit is therefore indicative of a (111)-type pit in a (100)-type surface, as can be rationalized using a model etch pit (Figure S28). In addition to these (111) sites, triangular and rectangular (100) pits are also visible in Figures S25c and 8d.

Pits are also observed after corrosion in 5 M NaOH, as is shown in Figure 8b. These features are larger than those seen for corrosion in 5 M LiOH, but match the orientation of (111)-type pits in (100)-type surfaces. The pits are accompanied by less well-defined roughness (Figure S26), but also by large, quasi-octahedral particles close to the tip of the electrode. These well-defined particles were previously observed after corrosion in 10 M NaOH and are strong indicators of the formation of (111) sites.[8,16]

Well-defined particles and pits were absent for 5 M KOH. Corrosion in this electrolyte predominantly caused the etching of crystal grains, leading to the disordered features in Figure 8c. In addition, cathodic corrosion created disordered particles (Figure 8f); these particles were exclusively present at the tip of the electrode, where it was cut from the spool. As such, the presence of these small, disordered particles and etch pits supports the suggestion that corrosion in 5 M KOH causes the formation of a more disordered type of gold surface.

Thus, SEM imaging reinforces the electrochemical observations for gold corrosion, indicating the following behaviors for the three electrolytes. First, 5 M LiOH is shown in both electrochemistry and electron microscopy to be the electrolyte in which the least surface area is created. When pronounced changes are present, both techniques can attribute them the formation of (triangular and rectangular) (100) sites and a small amount of (rectangular) (111) sites. Second, 5 M NaOH is shown electrochemically to create the most new surface area, consisting predominantly of (111) sites. This agrees well with the (111)-type etch pits and quasi-octahedral particles observed in SEM. Finally, 5 M KOH induces the formation of slightly more surface area than 5 M LiOH. This surface area appears to be disordered, as is indicated by the lack of well-defined oxide features in the first cycle after corrosion. The observed disorder is reflected in the SEM by the formation of many small etch pits and the presence of small nanoparticles at the tip of the electrode. As such, the combination of CV and SEM characterization paints a consistent picture of the corrosion behavior of gold in 5 M LiOH, NaOH, and KOH.

Computationally Derived Adsorption and Surface Energies. After having experimentally mapped the corrosion behavior of Pt, Rh, and Au, we exchange our experimental viewpoint for a computational perspective. From this perspective, we will first focus on the specific adsorption of alkali metal cations, followed by the surface energies of hydrogen-covered metals.

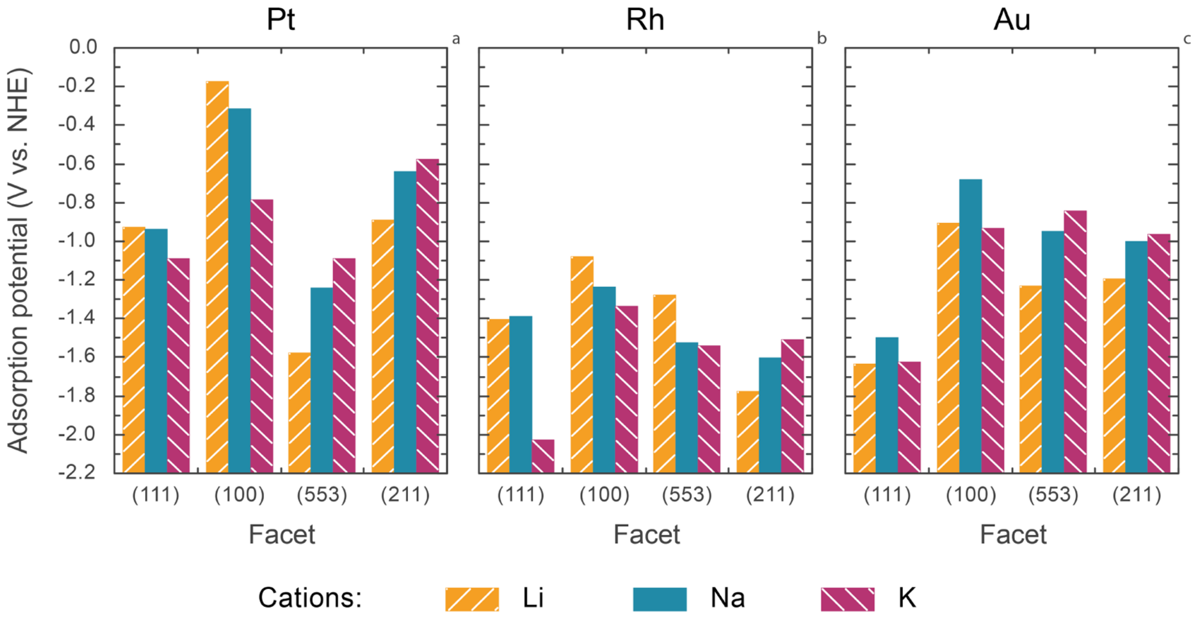

Figure 9. Equilibrium adsorption potentials for adsorption of Li, Na, and K on the (111), (100), (553), and (211) surfaces of Pt (a), Rh (b), and Au (c) from a 1 M solution of alkali metal cation.

Specific Adsorption of Cations. We will focus first on the specific adsorption of Li^+, Na^+, and K^+ on Pt, Rh, and Au. This approach extends from our work on sodium adsorption and initially considered adsorbed cations in vacuum, without including explicit solvation.[16] However, explicit near-surface solvation was previously shown to significantly affect cation adsorption.[28] Explicit solvation was therefore included in the results in the main text, whereas calculations without explicit solvation are shown for comparison in Figures S30 and S31. The presented calculations allowed us to calculate equilibrium adsorption potentials for cation adsorption, facilitating a direct comparison with the experimentally determined onset potentials.

Calculated equilibrium adsorption potentials for Li^+, Na^+, and K^+ onto the (111), (100), (553), and (211) facets of Pt, Rh, and Au are displayed in Figure 9. In this figure, cation adsorption is energetically favorable at potentials below the indicated equilibrium adsorption potential, as is signified by the bars covering the entire cation adsorption potential range. Although the cations transfer only a small part of their charge to the surface upon adsorbing, they do lose part of their solvation shell and interact directly with the metal surface. This therefore means that, within the context of this work, the cations are specifically adsorbed in the range covered by the bars in Figure 9.

Importantly, the adsorption range starts at less negative potentials than the onset potential of cathodic corrosion for most of the metal facets. Therefore, the cations are favorably adsorbed to the metal surface at potentials where cathodic corrosion occurs. As such, the results in Figure 9 support the importance of cation specific adsorption during cathodic corrosion. However, further assessment of the role of cations requires closer examination of adsorption trends across the different metal surface facets and between each of the alkali metal cations.

The trend in adsorption between facets is strongest for platinum (see Figure 9a): cation adsorption is weakest on (111)-type sites. This follows from the adsorption potential being most negative on the (111) and on the (553) facet.[53] This relatively weak binding to (111)-type sites is contrasted by adsorption on (100)-type sites: the least negative adsorption potentials are found for the (100) facet and the (211) facet.[54] This strong binding on (100) sites versus (111) sites might be related to the more open nature of (100)-type sites, which causes stronger binding for a variety of adsorbates.[55−57] Interestingly, this would imply an even stronger binding on step sites versus terrace sites, which is not observed. This apparent discrepancy is caused by a difference in cation coverage, as is discussed in more detail in the SI. Nonetheless, both Pt steps and terraces bind cations favorably to (100)-type sites, which correlates well with the experimentally observed preference for the creation of (100) sites on platinum.

While the adsorption energies for platinum show a clear trend that favors adsorption on (100) sites, there is no straightforward facet trend for Rh and Au (Figure 9b,c). Although these metals match Pt in exhibiting a strong preference for adsorption on (100) terraces over (111) terraces, they generally lack the significant difference between (553) and (211) that Pt exhibits.

Similarly, Pt is the only metal to exhibit clear trends in the calculated differences between cations. For Pt, steps and terraces behave oppositely; on terraces, Li adsorbs most strongly, followed by Na and K. In contrast, Pt steps adsorb K most strongly, followed by Na and Li. This difference between terraces and stepped surfaces arises from the different relative coverages of the cations on each surface, as is explained in the SI.

The trends with respect to cation identity for platinum are only partly upheld for Rh and Au: only the Rh(100), Rh(211), Au(553), and Au(211) trends behave similarly to their Pt counterparts. This absence of a calculated trend matches the experimental absence of a clear facet trend between cations for both Rh and Au.

Energies of Hydrogen-Covered Surfaces. In addition to examining alkali metal cation adsorption, we explored high coverages of adsorbed hydrogen, which may be present on Pt, Rh, and Au at cathodic corrosion potentials. We did so by calculating the surface energies of the (111) and (100) facets of Pt, Rh, and Au in the absence and presence of a monolayer (ML) of adsorbed hydrogen. These calculations were performed using values from literature DFT studies.[38,39] For (100) surfaces, we additionally found previously that the adsorption of as much as 1.25 monolayers of hydrogen is favorable at potentials near 0 V versus RHE.[42] These data were therefore included, and the surface energy extrapolated to lower potentials in Figure 10a. Similarly, high coverages were calculated in the current work for Rh(100) and are included in Figure 10b, since the hydrogen binding strength of Rh is similar to that of Pt. Because the calculations for 1.25 ML coverage on Pt(100) and Rh(100) used different protocols from the calculations of Ferrin et al., our results were added to the graph as separate lines. Interestingly, our DFT data in Figure 10 (dark purple) and calculations using literature values (pink) appear similar. This agreement inspires confidence in using Figure 10 as a first-order approximation of the stabilizing effect of adsorbed hydrogen.

Figure 10 indicates that, at potentials positive of hydrogen adsorption, the surface energy is constant as a function of potential. This constant energy is a result of ignoring electrolyte species like water or hydroxyl, which may adsorb to strongly binding surfaces and lower the overall surface energy at positive potentials. At more cathodic potentials, adsorbed hydrogen is calculated to be stable. These potentials generally correspond with hydrogen adsorption features in the blank cyclic voltammograms of platinum and rhodium and initiate a decrease in surface energy in Figure 10. This linear energy decrease is driven by hydrogen adsorption. This adsorption is increasingly favorable at lower potentials, which lowers the total energy of the system. Eventually, this constant decrease causes the surface energy to drop below 0 eV Å^{-2}, as compared to bulk metal. When this happens, the creation of more surface area to facilitate hydrogen adsorption is energetically more favorable than the breaking of Pt−Pt bonds that such creation of surface area would require.

Importantly, this surface energy transition occurs at potentials that match the experimental corrosion onset potentials: approximately −0.4 to −0.5 V versus RHE for Pt and Rh, and −0.7 V versus RHE for Au. (Exact potentials are given in Table S1.) Although it is important to emphasize that we calculated the curves in Figure 10 using literature data that was obtained using different DFT methodologies,[38,39] the curves match our experimentally determined onset potentials rather well. As such, Figure 10 indicates that high hydrogen coverages may be an energetic driving force for surface area creation and could therefore strongly affect the onset of cathodic corrosion.

DISCUSSION

Onset Potential. In the current work, we established onset potentials for cathodic corrosion of Pt, Rh, and Au in various concentrations of LiOH, NaOH, and KOH. Additionally, we explored the role of cation and hydrogen adsorption through theoretical calculations. Although this combination of theory and experiment does not unambiguously explain the nature of cathodic corrosion, it does provide valuable new clues toward elucidating this puzzling (electro)chemical phenomenon. Perhaps the most concrete of these clues are related to the onset potential of cathodic corrosion.

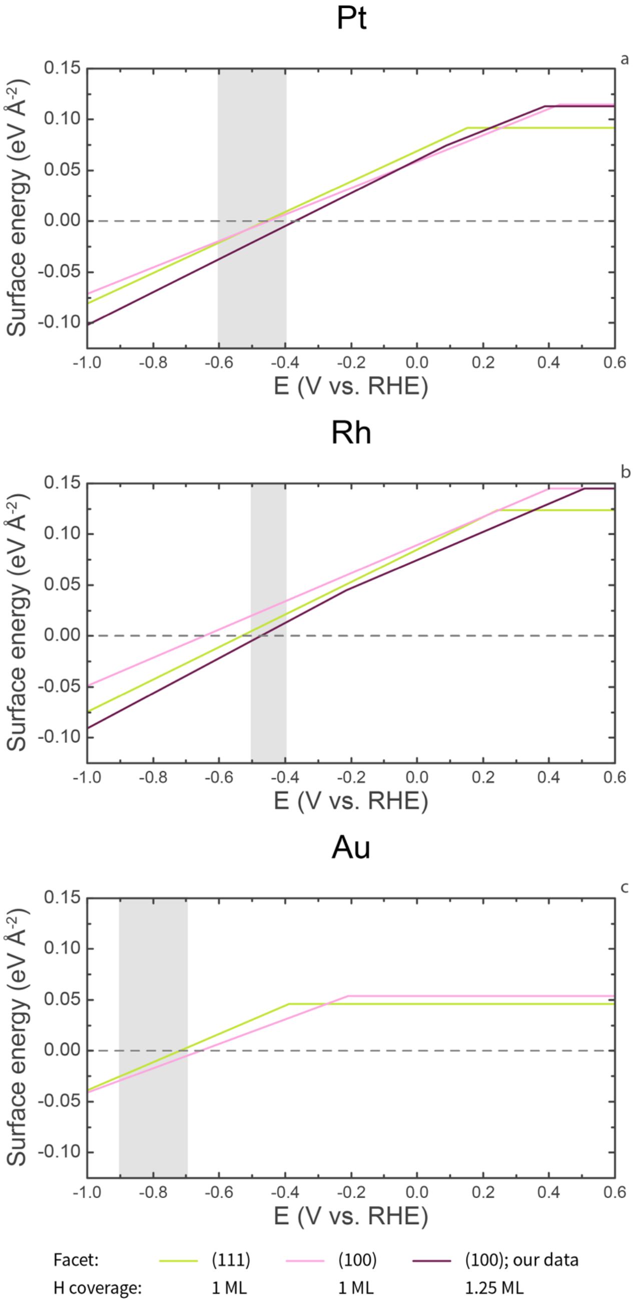

Figure 10. Potential-dependent surface energy of the (111) and (100) facets of Pt (a), Rh (b), and Au (c) in the absence and presence of 1 ML H*. On Pt(100) and Rh(100), we have additionally considered the adsorption of 1.25 ML H*. Our own data for Rh(100) was calculated with the PBE exchange-correlation functional instead of PW91. The range of experimentally determined onset potentials in our current and previous work is marked in gray.

The onset potential depends strongly on the electrolyte concentration: corrosion takes place at less negative potentials as the concentration increases. This trend is valid for Pt, Rh, and Au, as can be seen by comparing the current results with previous results in more concentrated electrolytes.[15,16] The corrosion onset is similarly sensitive to the nature of the electrolyte cation: it generally starts at the least negative potentials for K$^+$, followed by Na$^+$ and Li$^+$.

Although these experimental trends appear robust, they cannot conclusively be explained by the corresponding DFT results on cation adsorption. We therefore restrict this comparison of theory and experiment to two observations. First of all, larger cations are calculated to bind stronger to step edges. This could matter if cathodic corrosion were initiated at high-energy defect or step sites on the electrodes. Second, we calculate that larger cations retain more of their charge upon adsorption. This could shift the onset potential if cations were required to electrostatically stabilize an anionic reaction intermediate. Although speculative in nature, these computational suggestions parallel the observed effects of cations on the corrosion onset potential. These suggestions are therefore worthy of consideration in further mechanistic studies of cathodic corrosion.

In addition to the influence of cations on the corrosion onset, a similar role might be played by hydrogen: hydrogen is adsorbed on most metal surfaces at potentials where cathodic corrosion occurs. Exploring the effect of adsorbed hydrogen on the potential-dependent surface energy (Figure 10), we found an energetic driving force for the creation of surface area. This driving force appears at potentials that correspond remarkably well with the experimental cathodic corrosion onset potentials. Importantly, this agreement was established without making any kinetic or mechanistic assumptions: it simply indicates a thermodynamic driving force for creating more surface area around the corrosion onset potential.

The onset potential of cathodic corrosion therefore appears to depend on three major actors:

1. The corroded metal.
2. The electrolyte cation, which also affects various other factors of corrosion.[9−13,15,16]
3. Adsorbed hydrogen.

Given the pronounced effect of each of these actors on the location of the corrosion onset, it is likely that each of them is involved in creating the elusive intermediate species that underlies cathodic corrosion. A possible class of species that contains all three actors and has been observed experimentally is ternary metal hydrides.

In brief, ternary metal hydrides are compounds with the general formula $A_xM_yH_z$, where A is an alkali or alkaline earth metal and M is a transition metal.[58] In the solid state, these compounds contain anionic $[MH_n]^{\delta-}$ clusters, which are stabilized by surrounding cations.[59] As such, these hydrides contain both ionic (or Coulombic) interactions between the cation and the anionic cluster, and covalent (or coordination) bonds between the metal center and the hydrogen atoms.[60] A variety of these hydrides with Pt and Rh centers have been synthesized and fully characterized.[59,61] Although similar solid-state examples of ternary gold hydrides are unavailable, their existence is not unlikely: AuH_2^- and AuH_4^- have been generated with laser ablation,[62] and theoretical calculations suggest that such AuH_2^- clusters could be stabilized by alkali metal cations.[63] Given these examples of ternary hydrides of Pt, Rh, and Au, such compounds might be the elusive intermediate that underlies cathodic corrosion.

The presence of these species would match the suggested simultaneous importance of the corroded metal, electrolyte cations, and adsorbed hydrogen. However, ternary metal hydrides are extremely sensitive to moisture and air,[59,64] which would make them highly unstable in our working electrolyte. Interestingly, this instability is consistent with current and previous experimental results. After all, during cathodic corrosion, only the reacting material (e.g., Pt, Rh, Au) and produced material (e.g., corroded Pt, Rh, and Au surfaces and nanoparticles) have explicitly been identified: the intermediate species is highly unstable and has, as of now, escaped direct detection and chemical isolation.

In short, these hydrides are unstable enough to explain their elusiveness during experiments, yet have been studied and characterized to such an extent that their existence is plausible in our system. Additionally, they require the presence of a metal center, hydrogen, and a stabilizing cation. As such, these hydrides are, in our opinion, prime targets for future mechanistic studies of the reaction intermediates of cathodic corrosion.

Electrode Area and Facet Distribution. Besides considering these mechanistic considerations, it is instructive to evaluate the role of cations in the final surface structure of the corroded electrodes. This role is relatively clear when considering cation concentration: higher concentrations lead to more severe changes in the facet distribution and the amount of created surface area for Pt (Figures 1 and 2). Rh and Au behave similarly in that corrosion is rather mild at lower cation concentrations.

These effects of cation concentration appear to be thermodynamic in nature, meaning here that prolonged corrosion in dilute electrolytes is not likely to produce similar results as shorter corrosion in more concentrated electrolytes. This is illustrated by the corrosion of electrodes in 5 M NaOH for various amounts of time (Figure S32): the difference between 1 and 10 min of corrosion is minimal, if at all present. As such, the presented corroded electrodes appear to have reached a stable state and the differences in Figure 1 are strictly a consequence of the cation concentration.

Similar to the cation concentration, the cation identity also affects the final state of the corroded electrodes. However, this effect appears to vary with the applied potential. At the most negative potentials, both the facet distribution and surface area creation are strongly affected by the cation identity for all three metals.

The strongest trend in facet preference is observed for the corrosion of Pt: a monotonic (100) preference is observed when increasing the cation size in 1 M electrolyte concentrations. This trend is captured well by our DFT results, which indicate the strongest binding on (100)-type steps ((211) facets) for K, followed by Na and Li. This trend is matched by (110)-type steps ((553) facets), which might explain why more step sites and more general surface area are produced in 5 M KOH, compared to LiOH and NaOH. As such, the DFT results for cation adsorption agree well with the experimental corrosion behavior of Pt.

However, the calculated cation adsorption strengths match less well with the corrosion behavior of Rh and Au: they do not explain the observed facet distributions or why most area is created in NaOH. At best, the absence of a clear trend in DFT resembles the absence of a clear trend in experimental facet distribution. The lack of overlap between experiment and theory can be attributed to the calculations in Figure 9 only capturing cation adsorption. Other factors, like hydrogen adsorption, are not captured in these calculations. Cation adsorption therefore only partly determines the corrosion behavior at more negative potentials, and hydrogen co-adsorption might improve the predictions.

At milder negative potentials, the cation identity appears unimportant in determining the electrode structure for all three metals:

- For Pt, the CVs of electrodes that corroded at mildly negative potentials show great similarity (Figure 3), especially when comparing the amount of created (100) terraces. In addition, close comparison of the micrographs in Figures 2, 4, and S16−S21 reveals that the earliest indications of corrosion are typically (100)-oriented triangular etch pits, regardless of the identity and concentration of the electrolyte cation.
- For Rh, both the surface area increase and hydrogen desorption peak shift (Figure 5) are similar for all three electrolytes at mildly negative potentials (approximately −0.6 V vs RHE) before diverging at more negative potentials.
- For Au, the facet distribution after corrosion (Figure S29) is virtually identical for corrosion in both 5 M NaOH and KOH.

These observations suggest that the cation is of limited relevance in determining the electrode structure at mildly negative potentials, but of large significance at more negative potentials. This might be due to an increased adsorbed cation coverage at more negative potentials, as is explained in the SI. Such a coverage dependence might imply an interplay between both adsorbed cations and adsorbed hydrogen. This would be consistent with our mechanistic hypothesis regarding ternary metal hydrides.

Implications for Electrode Structuring. Regardless of the exact mechanisms that underlie the final structure of corroded electrodes, the current work provides a detailed characterization of the cathodic corrosion behavior of various combinations of electrode materials and electrolyte alkali metal cations. These results are particularly relevant when employing cathodic corrosion to alter the surface of metallic electrodes. Hence, we will end our discussion with recommendations for structuring electrodes by cathodic corrosion. The first three sets of recommendations are metal-specific:

- Platinum generally prefers forming (100) sites during cathodic corrosion. However, the extent of this preference can be significantly tuned by varying both the identity and concentration of the alkali metal cations in the electrolyte. The strongest preference for forming well-defined (100) terraces without creating steps is found for corrosion in 5 M NaOH. If LiOH is used instead, the corroded electrodes appear smoother in SEM (Figures 4, S16, and S19) and expose slightly less (100) terraces in voltammetry. Accordingly, changing the cation to K^+ induces the formation of a rougher and (at 5 M concentrations) more disordered surface.
- Rhodium exhibits a minor (100) preference, which is strongest in NaOH. NaOH is also the electrolyte of choice when a large surface area increase is desired. If less surface area and (100) preference are required, LiOH and KOH are more appropriate working electrolytes: corrosion in LiOH creates surfaces that appear in SEM to retain most of their original morphology, while KOH induces nanosized corrugation and slightly more roughness on the electrode.
- For gold, cathodic corrosion should be carried out at more negative potentials than for platinum and rhodium. When doing so, corrosion in LiOH creates electrodes with moderate roughening, exhibiting some well-defined (100) and (111) etch pits. More severe roughening is present after corrosion in NaOH, which creates most roughening and large (111)-oriented particles. Newly formed (111) sites are most clearly expressed in 10 M NaOH, where the (111) oxide peak can be quite well defined.[16] Finally, corrosion in KOH creates intermediate degrees of surface area, accompanied by corrugation along grain boundaries.

Finally, we will conclude our recommendations with three more general notes:

- Both the current and previous works indicate crystallographic preferences in cathodic corrosion:[15,16] clear facet preferences can be identified and corrosion appears most pronounced around grain boundaries and, in the case of unannealed Rh and Au electrodes, in areas close to where the electrodes were cut from the spool with wire cutters. This parallels previous findings in nanoparticle synthesis through cathodic corrosion, which achieved the most well-defined nanoparticles after prolonged annealing of the parent electrode.[12] The extent of corrosion may therefore vary, depending on the initial state of the electrode: more or less corrosion than found in the current work may be observed if mechanical stress is reduced by annealing or introduced by methods like mechanical polishing.
- Our recommendations are strictly valid in the studied potential range. Although more negative potentials will likely just emphasize the findings in the current work, exploring such potentials is encouraged when aiming to create an optimal surface structure. Similarly, if the target surface structure requires less corrosion, lower potentials can be chosen by consulting Figures S4−S27.
- Although the current work focuses on using pure alkali metal hydroxides to avoid overcomplicated analyses, different electrolytes might generate different and interesting results. Mixing cations to combine or balance their effects might be effective, as well as using entirely different cations. However, care should be taken not to choose cations that electrodeposit under the chosen corrosion conditions, to avoid the possible formation of metal overlayers or even alloy phases.[65]

■ CONCLUSIONS

The current work has explored the cathodic corrosion behavior of Pt, Rh, and Au in LiOH, NaOH, and KOH, to systematically assess the effect of the electrolyte cation. In doing so, it was found experimentally that both the concentration and identity of the cation can strongly affect the surface area and facet distribution of corroded electrodes, as well as the cathodic corrosion onset potential. These experimental results led to a set of concrete recommendations for employing cathodic corrosion to modify the structure of metallic electrodes for a specific purpose.

In addition to producing guidelines, we rationalized our experimental results by using first-principles calculations of cation adsorption. Importantly, the calculations indicate that cations are adsorbed at potentials where cathodic corrosion occurs. Although the calculations also satisfactorily reproduce the trend for (100) site formation for Pt in 1 M LiOH, NaOH, and KOH, they do not conclusively explain other trends in the onset potential, facet distribution, and surface area increase after cathodic corrosion. More mechanistic information on cathodic corrosion is therefore required to explain the strong effect of cations on these factors.

Equally relevant for the onset of corrosion is perhaps the adsorption of hydrogen; an analysis of literature hydrogen adsorption values indicates a thermodynamic driving force for the creation of surface area. Importantly, this driving force matches the experimental trend in onset potentials between metals, without making any mechanistic assumptions.

By combining the observed relevance of hydrogen, electrolyte cations, and the corroded electrode material, we postulate that the key reaction intermediate of cathodic corrosion might be a ternary metal hydride. Although the current work provides no direct evidence for such metal hydrides, their solid-state properties have been extensively studied and their occurrence would match several experimental observations. Notably, ternary metal hydrides would explain the importance of cations that has been explored in previous work and reaffirmed in the presented research. Ternary metal hydrides are therefore plausible reaction intermediates, which could serve as a starting point for further mechanistic studies of cathodic corrosion.

In conclusion, the current work on cathodic corrosion provides recommendations for electrode surface structuring, extensive information on the role of cations during direct current cathodic corrosion, and a testable hypothesis for the nature of the elusive cathodic corrosion reaction intermediate. As such, the work presented here is an essential step in both understanding and applying cathodic corrosion.

■ ASSOCIATED CONTENT

Ⓢ Supporting Information

The Supporting Information is available free of charge on the ACS Publications website at DOI: 10.1021/acsami.8b13883.

> Images of calculated DFT surface structures; cyclic voltammograms and scanning electron micrographs of each material/electrolyte combination after corrosion at various potentials, including more elaborate discussion; cartoons of model etch pits; normal and derivative voltammograms for gold onset determination; computational results for cation adsorption in vacuum; calculated potentials of zero surface energy; and cyclic voltammograms illustrating the effect of increased corrosion time (PDF)

■ AUTHOR INFORMATION

Corresponding Author

*E-mail: m.koper@lic.leidenuniv.nl.

ORCID

Thomas J. P. Hersbach: 0000-0001-5467-6151
Federico Calle-Vallejo: 0000-0001-5147-8635
Marc T. M. Koper: 0000-0001-6777-4594

Notes

The authors declare no competing financial interest.

■ ACKNOWLEDGMENTS

The authors thank Dr. Kathleen Schwarz at the National Institute of Standards and Technology, Dr. Dennis Hetterscheid at Leiden University, and Dr. Alex Yanson at Cosine Measurements for fruitful discussions on the nature of cathodic corrosion and the role of metal hydrides. In addition, the authors thank Rico Waanders, Shirley Wouters, and Marcin Talko for exploratory experiments. F.C.-V. acknowledges the Spanish MEC for a Ramón y Cajal research contract (RYC-2015-18996). The use of supercomputing facilities at SURFsara was sponsored by NWO Physical Sciences, with financial support by NWO. SEM measurements were performed in the shared clean room facility at the Leiden Institute of Physics.

■ REFERENCES

(1) Haber, F. The Phenomenon of the Formation of Metallic Dust from Cathodes. *Trans. Am. Electrochem. Soc.* **1902**, *2*, 189−196.

(2) Kabanov, B. N.; Astakhov, I. I.; Kiseleva, I. G. Formation of Crystalline Intermetallic Compounds and Solid Solutions in Electrochemical Incorporation of Metals into Cathodes. *Electrochim. Acta* **1979**, *24*, 167−171.

(3) Liu, J.; Huang, W.; Chen, S.; Hu, S. Facile Electrochemical Dispersion of Bulk Rh into Hydrosols. *Int. J. Electrochem. Sci.* **2009**, *4*, 1302−1308.

(4) Huang, W.; Chen, S.; Zheng, J.; Li, Z. Facile Preparation of Pt Hydrosols by Dispersing Bulk Pt with Potential Perturbations. *Electrochem. Commun.* **2009**, *11*, 469−472.

(5) Leontyev, I.; Kuriganova, A.; Kudryavtsev, Y.; Dkhil, B.; Smirnova, N. New Life of a Forgotten Method: Electrochemical Route toward Highly Efficient Pt/C Catalysts for Low-Temperature Fuel Cells. *Appl. Catal., A* **2012**, *431−432*, 120−125.

(6) Yanson, A. I.; Rodriguez, P.; Garcia-Araez, N.; Mom, R. V.; Tichelaar, F. D.; Koper, M. T. M. Cathodic Corrosion: A Quick, Clean, and Versatile Method for the Synthesis of Metallic Nanoparticles. *Angew. Chem., Int. Ed.* **2011**, *50*, 6346−6350.

(7) Gangal, U.; Srivastava, M.; Gupta, S. K. S. Mechanism of the Breakdown of Normal Electrolysis and the Transition to Contact Glow Discharge Electrolysis. *J. Electrochem. Soc.* **2009**, *156*, F131−F136.

(8) Strasser, P.; Gliech, M.; Kuehl, S.; Moeller, T. Electrochemical Processes on Solid Shaped Nanoparticles with Defined Facets. *Chem. Soc. Rev.* **2018**, *47*, 715−735.

(9) Yanson, A. I.; Antonov, P. V.; Rodriguez, P.; Koper, M. T. M. Influence of the Electrolyte Concentration on the Size and Shape of Platinum Nanoparticles Synthesized by Cathodic Corrosion. *Electrochim. Acta* **2013**, *112*, 913−918.

(10) Yanson, A. I.; Antonov, P. V.; Yanson, Y. I.; Koper, M. T. M. Controlling the Size of Platinum Nanoparticles Prepared by Cathodic Corrosion. *Electrochim. Acta* **2013**, *110*, 796−800.

(11) Feng, J.; Chen, D.; Sediq, A. S.; Romeijn, S.; Tichelaar, F. D.; Jiskoot, W.; Yang, J.; Koper, M. T. M. Cathodic Corrosion of a Bulk Wire to Nonaggregated Functional Nanocrystals and Nanoalloys. *ACS Appl. Mater. Interfaces* **2018**, *10*, 9532−9540.

(12) Duca, M.; Rodriguez, P.; Yanson, A. I.; Koper, M. T. M. Selective Electrocatalysis on Platinum Nanoparticles with Preferential (100) Orientation Prepared by Cathodic Corrosion. *Top. Catal.* **2014**, *57*, 255−264.

(13) Yanson, A. I.; Yanson, Y. I. Cathodic Corrosion. II. Properties of Nanoparticles Synthesized by Cathodic Corrosion. *Low Temp. Phys.* **2013**, *39*, 312−317.

(14) Peng, Z.; Yang, H. Designer Platinum Nanoparticles: Control of Shape, Composition in Alloy, Nanostructure and Electrocatalytic Property. *Nano Today* **2009**, *4*, 143−164.

(15) Hersbach, T. J. P.; Yanson, A. I.; Koper, M. T. M. Anisotropic Etching of Platinum Electrodes at the Onset of Cathodic Corrosion. *Nat. Commun.* **2016**, *7*, No. 12653.

(16) Hersbach, T. J. P.; Mints, V. A.; Calle-Vallejo, F.; Yanson, A. I.; Koper, M. T. M. Anisotropic Etching of Rhodium and Gold as the Onset of Nanoparticle Formation by Cathodic Corrosion. *Faraday Discuss.* **2016**, *193*, 207−222.

(17) Van de Krol, R. The Reference and Quasi-Reference Electrodes. In *Photoelectrochemical Hydrogen Production*; Van de Krol, R., Grätzel, M., Eds.; Springer, Boston, MA, 2012; p 109.

(18) Jeyabharathi, C.; Ahrens, P.; Hasse, U.; Scholz, F. Identification of Low-Index Crystal Planes of Polycrystalline Gold on the Basis of Electrochemical Oxide Layer Formation. *J. Solid State Electrochem.* **2016**, *20*, 3025−3031.

(19) Kresse, G. Ab Initio Molecular Dynamics for Liquid Metals. *J. Non-Cryst. Solids* **1995**, *192−193*, 222−229.

(20) Kresse, G.; Furthmüller, J. Efficiency of Ab-Initio Total Energy Calculations for Metals and Semiconductors Using a Plane-Wave Basis Set. *Comput. Mater. Sci.* **1996**, *6*, 15−50.

(21) Kresse, G.; Furthmüller, J. Efficient Iterative Schemes for Ab Initio Total-Energy Calculations Using a Plane-Wave Basis Set. *Phys. Rev. B* **1996**, *54*, 11169−11186.

(22) Perdew, J. P.; Burke, K.; Ernzerhof, M. Generalized Gradient Approximation Made Simple. *Phys. Rev. Lett.* **1996**, *77*, 3865−3868.

(23) Perdew, J. P.; Burke, K.; Ernzerhof, M. Generalized Gradient Approximation Made Simple [Phys. Rev. Lett. 77, 3865 (1996)]. *Phys. Rev. Lett.* **1997**, *78*, 1396−1396.

(24) Blöchl, P. E. Projector Augmented-Wave Method. *Phys. Rev. B* **1994**, *50*, 17953−17979.

(25) Kresse, G.; Joubert, D. From Ultrasoft Pseudopotentials to the Projector Augmented-Wave Method. *Phys. Rev. B* **1999**, *59*, 1758−1775.

(26) Monkhorst, H. J.; Pack, J. D. Special Points for Brillouin-Zone Integrations. *Phys. Rev. B* **1976**, *13*, 5188−5192.

(27) Bengtsson, L. Dipole Correction for Surface Supercell Calculations. *Phys. Rev. B: Condens. Matter Mater. Phys.* **1999**, *59*, 12301−12304.

(28) Mills, J. N.; McCrum, I. T.; Janik, M. J. Alkali Cation Specific Adsorption onto Fcc(111) Transition Metal Electrodes. *Phys. Chem. Chem. Phys.* **2014**, *16*, 13699−13707.

(29) McCrum, I. T.; Janik, M. J. PH and Alkali Cation Effects on the Pt Cyclic Voltammogram Explained Using Density Functional Theory. *J. Phys. Chem. C* **2016**, *120*, 457−471.

(30) Ogasawara, H.; Brena, B.; Nordlund, D.; Nyberg, M.; Pelmenschikov, A.; Pettersson, L. G. M.; Nilsson, A. Structure and Bonding of Water on Pt(111). *Phys. Rev. Lett.* **2002**, *89*, No. 276102.

(31) He, Z.-D.; Hanselman, S.; Chen, Y.-X.; Koper, M. T. M.; Calle-Vallejo, F. Importance of Solvation for the Accurate Prediction of Oxygen Reduction Activities of Pt-Based Electrocatalysts. *J. Phys. Chem. Lett.* **2017**, *8*, 2243−2246.

(32) Han, B.; Viswanathan, V.; Pitsch, H. First-Principles Based Analysis of the Electrocatalytic Activity of the Unreconstructed Pt(100) Surface for Oxygen Reduction Reaction. *J. Phys. Chem. C* **2012**, *116*, 6174−6183.

(33) Kolb, M. J.; Farber, R. G.; Derouin, J.; Badan, C.; Calle-Vallejo, F.; Juurlink, L. B. F.; Killelea, D. R.; Koper, M. T. M. Double-Stranded Water on Stepped Platinum Surfaces. *Phys. Rev. Lett.* **2016**, *116*, No. 136101.

(34) Momma, K.; Izumi, F. VESTA 3 for Three-Dimensional Visualization of Crystal, Volumetric and Morphology Data. *J. Appl. Crystallogr.* **2011**, *44*, 1272−1276.

(35) Varma, S.; Rempe, S. B. Coordination Numbers of Alkali Metal Ions in Aqueous Solutions. *Biophys. Chem.* **2006**, *124*, 192−199.

(36) Resasco, J.; Chen, L. D.; Clark, E.; Tsai, C.; Hahn, C.; Jaramillo, T. F.; Chan, K.; Bell, A. T. Promoter Effects of Alkali Metal Cations on the Electrochemical Reduction of Carbon Dioxide. *J. Am. Chem. Soc.* **2017**, *139*, 11277−11287.

(37) Pérez-Gallent, E.; Marcandalli, G.; Figueiredo, M. C.; Calle-Vallejo, F.; Koper, M. T. M. Structure- and Potential-Dependent Cation Effects on CO Reduction at Copper Single-Crystal Electrodes. *J. Am. Chem. Soc.* **2017**, *139*, 16412−16419.

(38) Tran, R.; Xu, Z.; Radhakrishnan, B.; Winston, D.; Sun, W.; Persson, K. A.; Ong, S. P. Surface Energies of Elemental Crystals. *Sci. Data* **2016**, *3*, No. 160080.

(39) Ferrin, P.; Kandoi, S.; Nilekar, A. U.; Mavrikakis, M. Hydrogen Adsorption, Absorption and Diffusion on and in Transition Metal Surfaces: A DFT Study. *Surf. Sci.* **2012**, *606*, 679−689.

(40) Karlberg, G. S.; Jaramillo, T. F.; Skúlason, E.; Rossmeisl, J.; Bligaard, T.; Nørskov, J. K. Cyclic Voltammograms for H on Pt(111) and Pt(100) from First Principles. *Phys. Rev. Lett.* **2007**, *99*, No. 126101.

(41) Skúlason, E.; Tripkovic, V.; Björketun, M. E.; Gudmundsdóttir, S.; Karlberg, G.; Rossmeisl, J.; Bligaard, T.; Jónsson, H.; Nørskov, J. K. Modeling the Electrochemical Hydrogen Oxidation and Evolution Reactions on the Basis of Density Functional Theory Calculations. *J. Phys. Chem. C* **2010**, *114*, 22374−22374.

(42) McCrum, I. T.; Hickner, M. A.; Janik, M. J. First-Principles Calculation of Pt Surface Energies in an Electrochemical Environment: Thermodynamic Driving Forces for Surface Faceting and Nanoparticle Reconstruction. *Langmuir* **2017**, *33*, 7043−7052.

(43) Koper, M. T. M.; Lukkien, J. J. Modeling the Butterfly: The Voltammetry of $(\sqrt{3} \times \sqrt{3})$R30° and p(2 × 2) Overlayers on (111) Electrodes. *J. Electroanal. Chem.* **2000**, *485*, 161−165.

(44) Garcia-Araez, N.; Lukkien, J. J.; Koper, M. T. M.; Feliu, J. M. Competitive Adsorption of Hydrogen and Bromide on Pt(100): Mean-Field Approximation vs. Monte Carlo Simulations. *J. Electroanal. Chem.* **2006**, *588*, 1−14.

(45) Solla-Gullón, J.; Rodríguez, P.; Herrero, E.; Aldaz, A.; Feliu, J. M. Surface Characterization of Platinum Electrodes. *Phys. Chem. Chem. Phys.* **2008**, *10*, 1359−1373.

(46) Chen, X.; McCrum, I. T.; Schwarz, K. A.; Janik, M. J.; Koper, M. T. M. Co-Adsorption of Cations as the Cause of the Apparent PH Dependence of Hydrogen Adsorption on a Stepped Platinum Single-Crystal Electrode. *Angew. Chem., Int. Ed.* **2017**, *56*, 15025−15029.

(47) McCrum, I. T.; Janik, M. J. First Principles Simulations of Cyclic Voltammograms on Stepped Pt(553) and Pt(533) Electrode Surfaces. *ChemElectroChem* **2016**, *3*, 1609−1617.

(48) Vidal-Iglesias, F. J.; Arán-Ais, R. M.; Solla-Gullón, J.; Herrero, E.; Feliu, J. M. Electrochemical Characterization of Shape-Controlled Pt Nanoparticles in Different Supporting Electrolytes. *ACS Catal.* **2012**, *2*, 901−910.

(49) Xu, Q.; Linke, U.; Bujak, R.; Wandlowski, T. Preparation and Electrochemical Characterization of Low-Index Rhodium Single Crystal Electrodes in Sulfuric Acid. *Electrochim. Acta* **2009**, *54*, 5509−5521.

(50) Štrbac, S.; Adžić, R. R.; Hamelin, A. Oxide Formation on Gold Single Crystal Stepped Surfaces. *J. Electroanal. Chem. Interfacial Electrochem.* **1988**, *249*, 291−310.

(51) Kibler, L. A. *Preparation and Characterization of Noble Metal Single Crystal Electrode Surfaces*; International Society of Electrochemistry, 2003.

(52) Trasatti, S.; Petrii, O. Real Surface Area Measurements in Electrochemistry. *Pure Appl. Chem.* **1991**, *63*, 711−734.

(53) The (553) Facet Contains 5-Atom Long (111) Terraces and (111) Steps to Which the Cation Adsorbs.

(54) The (211) Facet Contains 3-Atom Long (111) Terraces and (100) Steps to Which the Cation Adsorbs.

(55) Li, H.; Calle-Vallejo, F.; Kolb, M. J.; Kwon, Y.; Li, Y.; Koper, M. T. M. Why (1 0 0) Terraces Break and Make Bonds: Oxidation of Dimethyl Ether on Platinum Single-Crystal Electrodes. *J. Am. Chem. Soc.* **2013**, *135*, 14329−14338.

(56) Li, H.; Li, Y.; Koper, M. T. M.; Calle-Vallejo, F. Bond-Making and Breaking between Carbon, Nitrogen, and Oxygen in Electrocatalysis. *J. Am. Chem. Soc.* **2014**, *136*, 15694−15701.

(57) Calle-Vallejo, F.; Loffreda, D.; Koper, M. T. M.; Sautet, P. Introducing Structural Sensitivity into Adsorption−energy Scaling Relations by Means of Coordination Numbers. *Nat. Chem.* **2015**, *7*, 403−410.

(58) Firman, T. K.; Landis, C. R. Structure and Electron Counting in Ternary Transition Metal Hydrides. *J. Am. Chem. Soc.* **1998**, *120*, 12650−12656.

(59) Yvon, K.; Renaudin, G. Hydrides: Solid State Transition Metal Complexes. In *Encyclopedia of Inorganic Chemistry*; King, R. B., Crabtree, R. H., Lukehart, C. M., Atwood, D. A., Scott, R. A., Eds.; John Wiley & Sons, Ltd.: Chichester, U.K., 2006; Vol. *III*, pp 1814−1846.

(60) Orgaz, E.; Gupta, M. Chemical Bonding Features of the Ternary Alkali Metal Platinum and Palladium Hydrides. *Int. J. Quantum Chem.* **2000**, *80*, 141−152.

(61) Bronger, W.; Müller, P.; Schmitz, D.; Spittank, H. Synthese Und Struktur von Na2PtH4, Einem Ternären Hydrid Mit

Quadratisch Planaren PtH42-Baugruppen. *Z. Anorg. Allg. Chem.* **1984**, *516*, 35−41.

(62) Wang, X.; Andrews, L. Gold Is Noble but Gold Hydride Anions Are Stable. *Angew. Chem., Int. Ed.* **2003**, *42*, 5201−5206.

(63) Rahm, M.; Hoffmann, R.; Ashcroft, N. W. Ternary Gold Hydrides: Routes to Stable and Potentially Superconducting Compounds. *J. Am. Chem. Soc.* **2017**, *139*, 8740−8751.

(64) Suchanek, E.; Lange, N.; Auffermann, G.; Bronger, W.; Lutz, H. D. Raman Spectroscopic Studies on Palladium and Platinum Hydrido Complexes. *J. Raman Spectrosc.* **1999**, *30*, 981−986.

(65) Bennett, E.; Monzó, J.; Humphrey, J.; Plana, D.; Walker, M.; McConville, C.; Fermin, D.; Yanson, A.; Rodriguez, P. A Synthetic Route for the Effective Preparation of Metal Alloy Nanoparticles and Their Use as Active Electrocatalysts. *ACS Catal.* **2016**, *6*, 1533−1539.